Final Report

Project Title:	High-Efficiency Low-Cost Solar Receiver for use in a Supercritical CO_2 Recompression Cycle
Project Period:	09/01/12 – 12/31/15
Project Budget:	$3,150,316
Submission Date:	04/06/2016
Recipient:	Brayton Energy, LLC
Address:	75B Lafayette Street Portsmouth, NH 03842
Award Number:	DE-EE0005799
Project Team:	n/a
Principal Investigator:	Shaun Sullivan Senior Mechanical Engineer Phone: 603-205-6009 Email: sullivan@braytonenergy.com
Business Contact:	Jim Kesseli President Phone: 603-601-0450 x 202 Email: kesseli@braytonenergy.com
DOE Project Officer:	Tommy Rueckert Phone: (202) 586-0942 Email: thomas.ruekert@ee.doe.gov
DOE Tech. Manager:	Andru Prescod Phone: (202) 287-1949 Email: andru.prescod@ee.doe.gov

Executive Summary

This project has performed solar receiver designs for two supercritical carbon dioxide (sCO_2) power cycles. The first half of the program focused on a nominally 2 MW_e power cycle, with a receiver designed for test at the Sandia Solar Thermal Test Facility. This led to an economical cavity-type receiver. The second half of the program focused on a 10 MW_e power cycle, incorporating a surround open receiver. Rigorous component life and performance testing was performed in support of both receiver designs. The receiver performance objectives are set to conform to the US DOE goals of 6¢/kWh by 2020[i]. Accomplishments are shown in Table 1. Key findings for both cavity-type and direct open receiver are highlighted below:

- A tube-based absorber design is impractical at specified temperatures, pressures and heat fluxes for the application; a plate-fin architecture however has been shown to meet performance and life targets.
- The \$148/kW_{th} cost of the design is significantly less than the SunShot cost target with a margin of 30%.
- The proposed receiver design is scalable, and may be applied to both modular cavity-type installations as well as large utility-scale open receiver installations.
- The design may be integrated with thermal storage systems, allowing for continuous high-efficiency electrical production during off-sun hours.
- Costs associated with a direct sCO_2 receiver for a sCO_2 Brayton power cycle are comparable to those of a typical molten salt receiver.
- Lifetimes in excess of the 90,000 hour goal are achievable with an optimal cell geometry.
- The thermal performance of the Brayton receiver is significantly higher than the industry standard, and enables at least a 30% efficiency improvement over the performance of the baseline steam-Rankine boiler/cycle system.
- Brayton's patent-pending quartz tube window provides a greater than five-percent efficiency benefit to the receiver by reducing both convection and radiation losses.

Table 1 – Brayton Energy SunShot program targets and results.

		CAVITY RECEIVER		EXTERNAL RECEIVER	
PERFORMANCE METRIC	**SUNSHOT TARGET**	**BRAYTON TARGET**	**BRAYTON RESULTS[1]**	**BRAYTON TARGET**	**BRAYTON RESULTS[2]**
Receiver Creep Life	n/a	≥ 90,000 hours	60,000 hours	≥ 90,000 hours	90,000 hours
Receiver Fatigue Life	≥ 10,000 cycles	≥ 10,000 cycles	≥ 100,000 cycles	≥ 10,000 cycles	≥ 100,000 cycles
Receiver Cost	≤ \$150/kW_{th}	≤ \$120/kW_{th}	\$98/kW_{th}	≤ \$150/kW_{th}	\$124/kW_{th}
HTF Exit Temeprature	≥ 650 ^{o}C	≥ 750 ^{o}C	750 ^{o}C	715 ^{o}C	715 ^{o}C
Receiver Efficiency $\eta_{thermal}$	n/a	≥ 95%	94.9%	*(partner defined)*	90.62%
Receiver Efficiency $\eta_{annualized}$	≥ 90%	≥ 92%	93.1%	*(partner defined)*	88.36%
System Efficiency Gain	-	-	-	≥ 15.00%	30.30% (10.27 pts.)
Quartz Window Benefit	-	-	-	≥ 2.00%	5.50% (6.10 pts.)

[1] Results as of the end of Phase 2; Cost does not include tower costs [2] Costs include tower costs

Table of Contents

Introduction

A compact, low-cost, high-efficiency extended-surface solar receiver for supercritical carbon dioxide (sCO_2) offers the greatest economic potential for concentrated solar power (CSP). The receiver designed in this program, combined with the sCO_2-Brayton recompression offers the highest efficiency potential among all CSP technologies; with a potential target of 50% solar-electric conversion efficiency ($\eta_{\text{receiver}}\ x\ \eta_{\text{power cycle}}$). Furthermore the capital cost analysis of the power conversion system supports the DOE target of 6¢/kWh.

Fundamental challenges of performance, cost, and life are addressed in the advanced receiver design described herein. The receiver design incorporates a number of innovative and unique characteristics that differentiate it from commercial CSP receiver designs. These include:

- A close-coupling between the tower-mounted turbomachinery and receiver. This significantly lowers installation and site engineering costs, while minimizing piping losses.
- Very high heat transfer performance is achievable using sCO_2 as a working fluid in the micro-channel absorber. This permits operation at high solar flux, this reduces the receiver size and cost.
- A patent-pending low-cost quartz window design, which effectively halves the radiation losses to ambient, resulting in a higher receiver efficiency. This is critical for efficient operation at elevated temperatures over 750°C, well above the current state-of-the-art.
- Conventional alloys (Alloy-625) combined with demonstrated automated manufacturing methods are shown to achieve a receiver cost < $124/kW$_{th}$, tower costs inclusive.
- The modular, factory assembled receiver lowers field installation cost, and serves a wide range of power plant sizes.

Project Results and Discussion

Milestones

Project milestones are given in Table 2. The precise scope of the project effort evolved over the course of the program, with SOPO modifications being made at the end of each phase. However, receiver performance metrics have all been met or surpassed, and analytical results have been validated through experimental testing of critical components and a suitable assembly test section.

Table 2 – Milestone Table for Program DE0005799: High-Efficiency Low-Cost Solar Receiver for use in a Supercritical CO_2 Recompression Cycle.

Mile stone	Metric	Success Value	Assessment Tool	Results	Notes
1.1.1	sCO_2 engine cycle model	Conversion efficiency ≥50% at design point	na	Cavity Receiver Design: 54% design point conversion efficiency Commercial Recevier Design: 50% design point conversion efficiency	Cavity Receiver: Receiver conditions (25 Mpa, 750 C at outlet) were selected to produce 54% efficiency for net 50% electric:solar conversion efficiency Commercial Receiver: Receiver conditions (25 Mpa, 715 C at outlet) were specified by commercial partner for 50% design point conversion efficency cycle
1.1.2	Absorber Cell Model	≤ 850°C max temperature ≤ 5% dP/P ≥ 40,000 hours life	Finite difference model, creep life predictions	Absorber cell architecture and receiver layout specified to maintain surface temperature below 800C and pressure drop below 5%. At temprature and pressure material strength is adequate for > 40,000 hours life	
1.2.1	Absorber Cell Samples	50 Mpa Internal Pressure	Hydrostatic pressure testing	Absorber cell architectures demonstrated to withstand up to 100 MPa	
1.2.2	Absorber Cell Cost Model	< $30/kW at high volume			
1.2.3	Receiver Cavity Shape Selection	850°C max wall temp	Conjugate finite difference heat transfer model	4.5 m long cylinder with 1.5 meter aperture diameter selected. Conjugate heat transfer model indicates surface tempratures within cavity remain below 800 C	
1.3.1	Decide on rotating vs. stationary receiver	Compare life vs. cost and complexity	Conjugate finite difference heat transfer model	STATIONARY	Benefit from flux leveling does not justify complexity; stationary absorber cells shown to maintain surface temperatures below 800 C throughout annual and diurnal flux
1.3.2	Receiver Life	Fatigue Life > 10,000 cycles Creep life > 40,000 hrs	Material-based creep life modeling	Creep Life = 90,000 hours Fatigue Life > 1,000,000	
1.4.1	Life of 10,000 thermal cycles and 90,000 operational hours	1) Perform 10,000 pressure cycles. (3 samples) 2) Perform testing at elevated temperature and pressure, applying Larson-Miller methodology. (3 samples)	Component testing via: 1) automated pressure cycling rig 2) creep test rig.	Creep Life > 90,000 hours Fatigue Life > 1,000,000	
2.1.1	2 MW_{th} Cavity Receiver Annualized efficiency	> 92%		93.5% (+0.7/-1.7%)	50
2.1.2	2 MW_{th} Cavity Receiver design with predicted high-volume production cost	< $120/kW$_{th}$			
2.2.1	Commercial Recevier Design	annualized efficiency > 90% > 90,000 hour creep life >10,000 cycle fatigue life < $110/kWth LCOE < 0.85* LCOE steam cycle		annualized efficiency=90.7% 60,000 hour creep life >100,000 cycle fatigue life $98/kWth	
2.2.2	sCO_2 Receiver Cost	Cost Benefit as compared to molten salt receiver for systems with a capacity factor between 10 and 90 %		Capital cost of sCO2 system comparable to that of molten salt; operational benefits (parasitics, efficiency or heliostat field size, etc.) anticipated to recommend	
2.3.1	Commercially attractive sCO_2 receiver design	Techncal memo with competitive cost at 100 MW_e/yr production			
2.3.2	Commercial viability	Letter of Interest from OEM parter			
2.4.1	Brayton to host meeting to present receiver assembly test options to DOE and SNLA	Consensus within the group	Go-To-Meeting		
2.4.2	Deliver final test plan for economical test within stated budget	$198,884	Budgetary quote from SNLA and Brayton		
3.1.1	Letter of Interest from established industrial partner	na	na		
3.2.1	The window shall show a >2% efficiency benefit. The following definition for efficiency will be applied to the receiver design with and without the window. $\eta = \frac{\dot{m}c_p(T)(\Delta T_{HTF})}{\dot{Q}_{aperture}} = \frac{\text{Heat transferred to HTF (MW)}}{\text{Solar radiation incident on aperture (MW)}}$	2% efficiency improvement	Experimental test	>5.5 pts. Efficiency improvement (combined convection and radiation)	
3.3.1	Receiver design achieves partner-specified performance, durability and cost criteria. The product of receiver and engine cycle efficiency shall show a 15% efficiency improvement. The following definition for efficiency will be applied to the baseline (from SAM) steam-Rankine and Brayton's receiver sCO_2 system. The net efficiency included all parasitics. $\eta = \frac{We}{\dot{Q}_{aperture}} = \frac{\text{Net Electric power delivered to the grid (MW)}}{\text{Solar radiation incident on aperture (MW)}}$	15% net efficiency improvement	Analytical models and SAM		

Previous Efforts

This section summarizes investigative efforts performed throughout this program. Additional details on each topic may be found in the quarterly and continuation reports generated.

Cycle Modeling

The cycle statepoints and operating efficiency (Table 4) for a cavity receiver using a sCO_2 recompression cycle were specified using the work of Dostal et. al[ii]. (54% Thermal-electric, 50% Solar-electric). For the external, surround-field, receiver configuration, the power block uses cycle performance metrics reported by GE (50% thermal-electric). The change was made due to limitations in the size of the cavity receiver, which can be roughly $2MW_{th}$ maximum, whereas an external receiver can be much larger. The GE sCO_2 power block is rated for $20MW_{th}$ input.

Table 3 – Cycle statepoints for cavity receiver and 54% efficient engine cycle.

RECEIVER PARAMETER	UNITS	VALUES
Mass Flow	kg/s	8.98
Inlet Temperature	°C	575
Inlet Pressure	MPa	25.75
Thermal Input	MW_{th}	2.00
Allowable Pressure Drop	%	3.0%
Outlet Pressure	Mpa	25.00
Outlet Temperature	°C	750

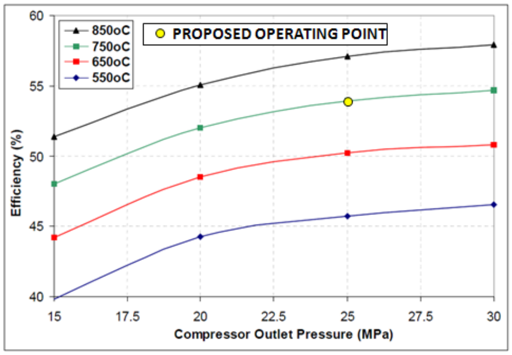

Figure 1 – sCO_2 recompression cycle efficiency vs. pressure and peak temperature.

Optical Modeling

Brayton developed and calibrated a solar heliostat field model for Sandia National Lab using NREL's SolTrace[iii] program. The model accounts for aiming errors, slope error, and specularity. The optical model was compared with flux data captured at Sandia. Errors were adjusted to match the measured power through a 1.5m diameter cavity receiver aperture located at 64m elevation. The calibrated model was used to generate flux profiles on the receiver (Figure 2) and perform cavity receiver optimization studies with the sun located at the solar equinox.

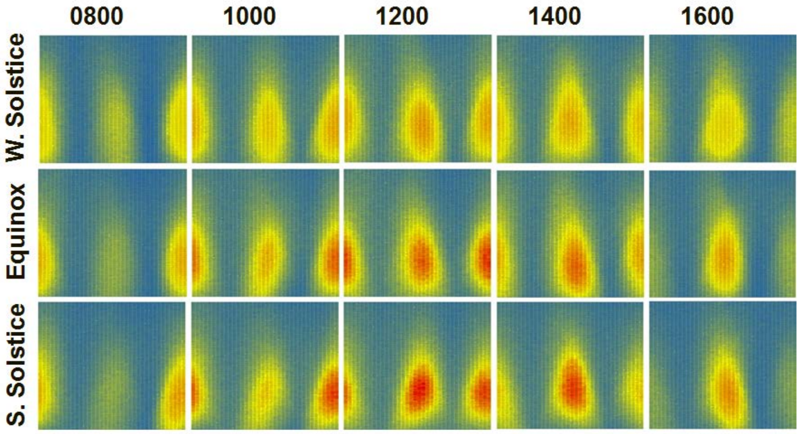

Figure 2 – Mercator projections of incident flux profiles on cavity receiver absorber surface through annual and diurnal solar variations.

Absorber Cell Modeling

Initial studies focused on a circular tube design with internal features (wire mesh or internal fin) to enhance convective heat transfer. These designs were deemed unsatisfactory due to either large pressure drop per unit length (wire mesh) or insufficient creep-fatigue life due to strains generated by through-wall temperature differences from concentrated solar heat flux acting on thick walls.

Diurnal flux variations and more frequent cloud passing events produce strain reversals with creep relaxation with premature failure predicted..

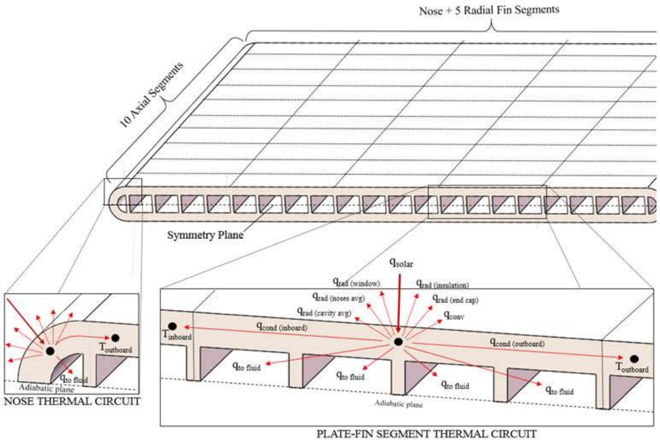

Figure 3 – Schematics of the plate-fin panel and the finite difference first-law energy balance terms.

A novel plate-fin construction (Figure 3) was conceived to allow a thin-walled pressure and heat-flux boundary by distributing pressure support over tightly spaced fins. This structure serves an equally important role in augmenting heat transfer with smaller hydraulic diameters and extended heat transfer area. The symmetry model assumes flux is incident on both faces of the absorber panel with the center plane treated as an adiabatic surface. The panel is divided into ten axial segments. At the radially inboard end, the "nose" of the cell faces into the incoming flux, and is treated as its own flow channel with a unique hydraulic diameter. The width of the plate-fin construction is divided into five equal segments, each containing a length of the plate-fin matrix. The six parallel flow channels (nose and 1 – 5) are fed by the same inlet pressure, and exhaust to the same discharge pressure. Mass flux through each passage is a product of fluid conditions and passage geometry. The outer plates of the six channels are in continuous thermal contact, allowing heat to conduct from hotter elements into cooler neighbors. The energy balance on each element node includes ten different heat flow terms, listed below:

- Solar flux incident on element
- Convection to fluid
- Radiation to endcap
- Radiation to backing insulation
- Radiation to aperture (quartz window)
- Convection to an average receiver cavity temperature
- Conduction through plate to adjacent inboard element
- Radiation to an average nose temperature
- Radiation to an average absorber panel temperature

System Modeling

The initial proposed sCO_2 receiver was a cavity receiver, similar in nature to other air-Brayton designs tested by Brayton Energy, Lockheed, Allied Signal, Boeing and university groups. The generally accepted efficiency prediction method segregates receiver losses into four categories: (1) Radiation loss, (2) Cavity convection losses, (3) External shell conduction losses, and (4) reflection losses. A combination of empiricism and analytical methods were used to estimate these losses.

- **Radiation** is the dominant loss in high temperature receivers Temperature within the cavity is not uniform resulting in radiation losses derived from the temperature and geometric view factor of each absorber element to the aperture. The radiation losses can be significantly reduced by the inclusion of an optical window. As illustrated in Figure 4, the quartz absorbs long wavelength emissions from the cavity, while transmitting the visible solar input power.
- **Cavity convection** is driven by the buoyancy of hot air within the receiver cavity. Brayton has conducted experiments to support correlations employed to predict this heat loss mechanism. Our testing has shown that the aforementioned tubular quartz window has no

significant impact on the convective heat loss at high tilt angles (near horizontal). At inclinations approaching vertical (downward facing cavity), the quartz bundle significantly reduces cavity convection losses.

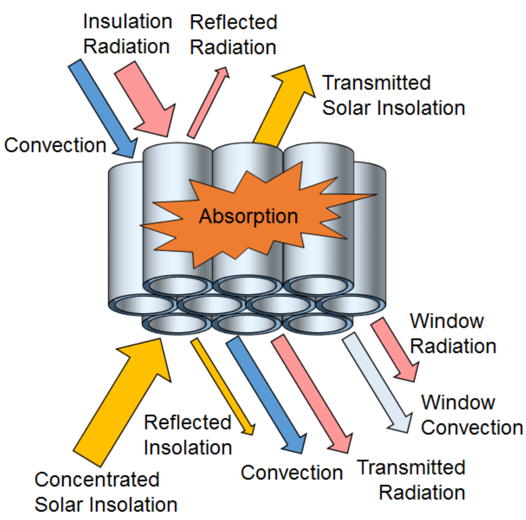

Figure 4 – Quartz window schematic showing the transmission of solar energy into the system, and the absorption of long-wave infrared radiation.

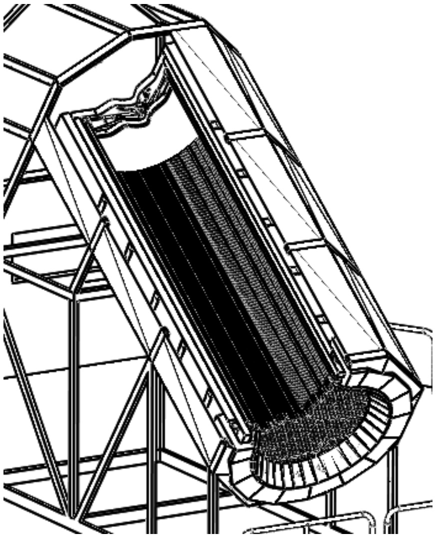

Figure 5 – Overall cavity receiver layout, showing cylindrical absorber tilted towards a south-facing heliostat field.

- **Cavity reflection** losses are present in all receivers, cavity or open. Cavity receivers are generally effective in capturing diffusely reflected rays incident on their high surface area interior. The current cavity design employs both reflective and absorbing surfaces. Reflective insulation on the 'roof' of the cavity and between the absorber elements serves to level the interior power distribution.
- **Shell conduction losses** represent heat loss emitted from the exterior of the insulated receiver vessel. This category is referred to as a conduction loss because the loss is dominated by the resistance of thermal insulation. A free convection heat transfer coefficient and a radiative emissivity are applied to the exterior of the insulated vessel. Despite large error bars on some of the conduction losses, the dominant effect of the insulation keeps the maximum losses to only a few kilowatts.

Rotation of the receiver was considered as a means of leveling the temperature distribution to gain efficiency and avoid thermo-mechanical strain. However, analytical findings show that metal temperatures in the peak-flux regions remain within acceptable bounds without consideration of radiation leveling or passive mass flux apportionment. The complexity and cost of rotating the receiver was deemed un-necessary.

Cavity Receiver Analysis and Design

A full cavity receiver layout was defined, with manifolds, structural support, insulation, and quartz window incorporated. Close-up images of this layout can be seen in Figure 6 and Figure 7.

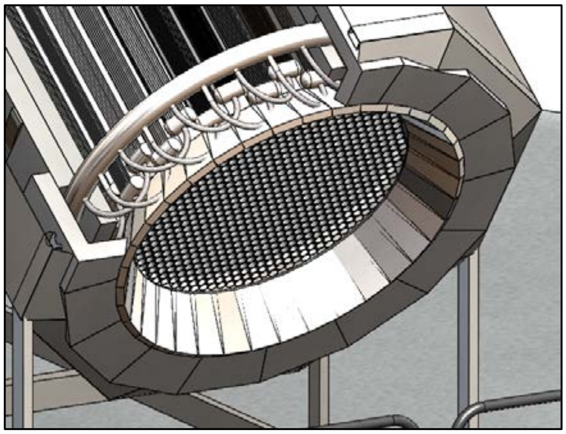

Figure 6 – Close-up of cavity receiver aperture, showing insulation face and quartz window details.

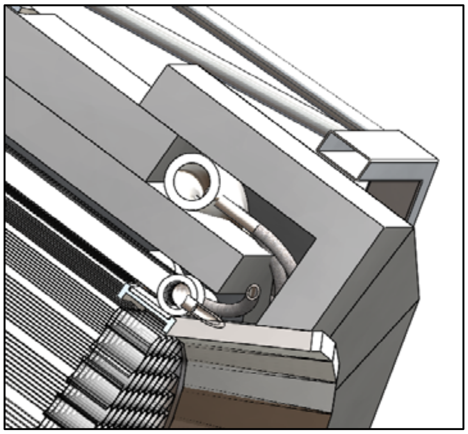

Figure 7 – Cutaway of cavity receiver aperture end, showing fluidic connections between panel and manifold.

The receiver finite-difference fluid-thermal model requires inputs for receiver geometry, cell flux distribution, heat transfer fluid flow distribution, inlet fluid properties, and an estimate of receiver efficiency. These input parameters implicitly prescribe the fluid enthalpy rise to attain a prescribed outlet temperature of 750°C. The thermal-fluid model performs an energy balance at several hundred discrete nodes within representative panels to determine the absorber metal temperatures required to attain the needed heat transfer within the system. The model further calculates the HTF pressure drop for each parallel flow channel within the receiver, taking into account the pressure drops corresponding to valves. The following analytical steps lead to a receiver performance prediction:

Table 4 – Calculated deviations in receiver efficiency on the basis of reasonable input errors.

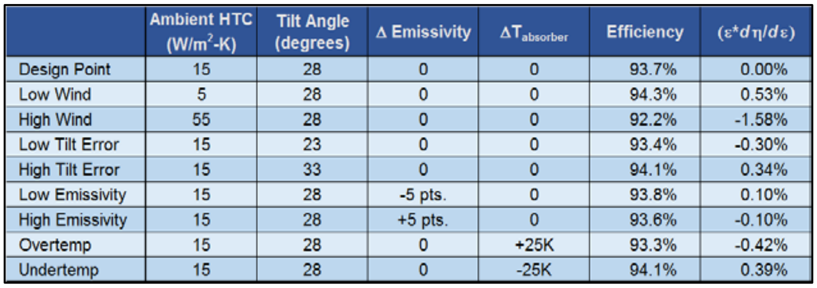

	Ambient HTC (W/m^2-K)	Tilt Angle (degrees)	Δ Emissivity	$\Delta T_{absorber}$	Efficiency	($\varepsilon * d\eta / d\varepsilon$)
Design Point	15	28	0	0	93.7%	0.00%
Low Wind	5	28	0	0	94.3%	0.53%
High Wind	55	28	0	0	92.2%	-1.58%
Low Tilt Error	15	23	0	0	93.4%	-0.30%
High Tilt Error	15	33	0	0	94.1%	0.34%
Low Emissivity	15	28	-5 pts.	0	93.8%	0.10%
High Emissivity	15	28	+5 pts.	0	93.6%	-0.10%
Overtemp	15	28	0	+25K	93.3%	-0.42%
Undertemp	15	28	0	-25K	94.1%	0.39%

1. Iteratively run SolTrace to determine DP heliostat subset (Field Multiple = 1) and receiver tilt angle to minimize "Power Factor" on cylindrical cavity surface
2. Locate maximum, minimum, and average power panels within the cylindrical panel array, and run SolTrace to determine flux distribution on these panels
3. Using simplified fluid-thermal model, estimate initial flow distribution (porting and valving) to levelize temperatures (panel-to-panel differences in max metal temp)
4. Iteratively run finite-difference thermal-fluid model, adjusting panel geometry and flow distribution to minimize panel temperatures within pressure drop budget
5. Using cavity temperatures from thermal-fluid model as inputs, run the cavity loss model to determine receiver efficiency

The analytical steps for determining the annualized receiver efficiency, which account for performance at each off-design case of the year, are the same as those used to determine the design point efficiency, using appropriate inputs for the heliostat selection, DNI, solar position, flow, and valve resistances corresponding to each case. However, these steps (1 – 5 above) must be repeated over a small representative subset of seasonal and diurnal intervals, and the resulting efficiencies must be appropriately weighted to give a reasonable estimate of “annualized efficiency.” From a computational perspective, a minimum number of analyses are needed to provide a desired accuracy. Analytical steps and related assumptions made in analyzing annualized receiver efficiency are summarized below.

- A Field Multiple of 1.2 is representative of typical solar installations. All heliostat selections for diurnal and seasonal times must be subsets of the FM 1.2 field.
- Smoothing or averaging of data from multiple years is required to properly account for atmospheric and cloud attenuation for a given day or set of days
- A lower DNI threshold exists, below which the solar plant will not operate. (Assumed for this study to be ~400 W/m2)
- Multi-year averaged time plots of seasonal DNI are of sufficiently regular shape that the year may be discretized into four representative and equal time blocks centered at: Vernal equinox, Summer solstice, Autumnal equinox, and Winter solstice
- Summer solstice and winter solstice may be used as bracketing maximum and minimum solar input (power) season-days. Inaccuracies introduced by this paired assumption are offsetting
- Vernal and autumnal equinox season-days may be considered identical, and inaccuracies owing to differing meteorological conditions may be discounted
- Receiver efficiency for a given time of a single day must be weighted according to total daily insolation (MW-h) when calculating daily receiver efficiency (energy-based weighting, not time-based weighting)
- Multi-year averaged time plots of daily DNI are of sufficiently regular shape that any day may be discretized into three representative blocks: AM, NOON, and PM, representing approximately 20%, 60%, and 20% of the day, respectively.

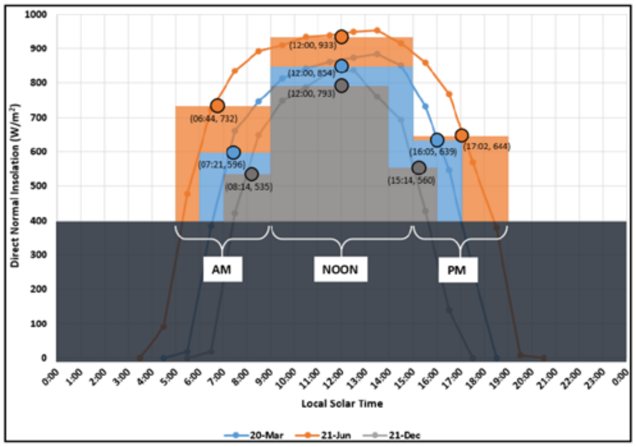

Figure 8 – Reduced season-day cases overlaid on DNI curves for Barstow, CA.

- For representative AM, NOON, and PM blocks in a given day, the average DNI may be determined for that block, and solar angle at that DNI may be used as a suitable average for optical modeling of each
- Receiver efficiency for a representative season-day of a single reference year must be weighted according to total annual insolation (MW-h) when calculating annualized receiver efficiency (energy-based weighting, not time-based weighting)
- For purposes of receiver efficiency weighting, both daily and seasonally, DNI (weighted by field cosine losses) is an appropriate surrogate for power available at the receiver aperture

Table 5 – Season-day cases and associated efficiency weightings

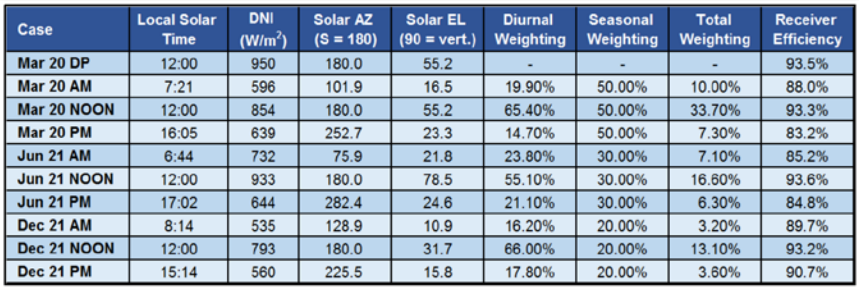

Case	Local Solar Time	DNI (W/m^2)	Solar AZ (S = 180)	Solar EL (90 = vert.)	Diurnal Weighting	Seasonal Weighting	Total Weighting	Receiver Efficiency
Mar 20 DP	12:00	950	180.0	55.2	-	-	-	93.5%
Mar 20 AM	7:21	596	101.9	16.5	19.90%	50.00%	10.00%	88.0%
Mar 20 NOON	12:00	854	180.0	55.2	65.40%	50.00%	33.70%	93.3%
Mar 20 PM	16:05	639	252.7	23.3	14.70%	50.00%	7.30%	83.2%
Jun 21 AM	6:44	732	75.9	21.8	23.80%	30.00%	7.10%	85.2%
Jun 21 NOON	12:00	933	180.0	78.5	55.10%	30.00%	16.60%	93.6%
Jun 21 PM	17:02	644	282.4	24.6	21.10%	30.00%	6.30%	84.8%
Dec 21 AM	8:14	535	128.9	10.9	16.20%	20.00%	3.20%	89.7%
Dec 21 NOON	12:00	793	180.0	31.7	66.00%	20.00%	13.10%	93.2%
Dec 21 PM	15:14	560	225.5	15.8	17.80%	20.00%	3.60%	90.7%

The annualized receiver efficiency was found to be 90.7%. If the receiver efficiency for the given solar conditions is recalculated based on the assumption of a cooler endcap (in a range of 720-1000°C), the resulting annualized efficiency would further increase to 93.4%.

Commercial Receiver

Four goals drove the development of the external direct-to-sCO_2 receiver design proposed by Brayton Energy, the latest evolution of which is detailed in a following section. These are:

- Incorporating the novel cell absorber element design, which is capable of reacting the extreme high pressures of a sCO_2 cycle while simultaneously providing high-effectiveness heat transfer; this feature, combined with the orientation that allows incident insolation to distribute over most of the cell perimeter, minimizes the irradiated material temperature and enables a long-life design.
- Arranging the cells into modular panels, which are spaced such that there is a minimal view factor between the passive high-temperature insulation and the environment, thereby reducing losses.
- Incorporating the novel Brayton-developed low-cost quartz tube bundle window design; the efficacy of this configuration, which leverages advantageous view factors between high-temperature surfaces and the environment, has been shown to significantly reduce radiation losses to the environment.
- Developing the entire module with the intention of making it factory-buildable and shippable via over-road transportation.

In pursuit of these goals, Brayton has defined the modular panel architecture shown in Figure 9. A pair of headers (with either convex or concave hemispherical endcaps, as the arrangement requires are connected by a series of parallel cells. These cells are welded at each end into headers using a process which has been successfully demonstrated. A passive insulation board appropriate for the conditions is mounted on the backside of the panel.

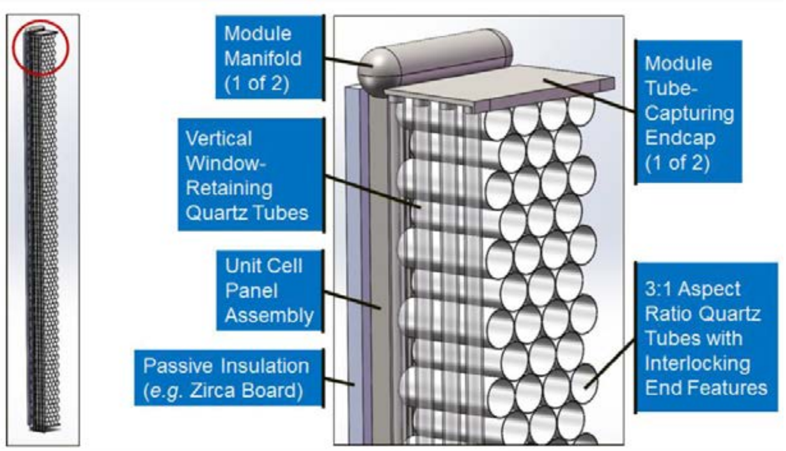

Figure 9 – Modular external receiver panel design.

Multiples of this absorber module can then be arranged around the circumference of a circle, extending both above and below the equator. By introducing receiver inlet fluid at the equator the lowest temperature fluid may be used to cool the highest-flux regions. This produces an outward-facing absorber surface with passive backing insulation and a low-cost quartz window that serves to reduce the radiation losses associated with the elevated surface temperatures of the receiver.

Solar Test Plan

Various on-sun test concepts have been developed for the purpose of evaluating the operational efficacy of a full absorber panel assembly. Although on-sun testing was not ultimately pursued under this program, plans developed suggest possibilities available in the future to be performed in conjunction with an industrial partner.

In its most favorably economic implementation, the test article will comprise three pre-heater panels and one high temperature test panel. The panels will be mounted within a water cooled structure with flow channels made of square tubing, similar to the water cooled surfaces of the Sandia tower. The panels will be mounted to accommodate relative thermal expansion and prevent panel buckling. All four panels will be backed by a passive insulation board, with a quartz window on the single test cartridge. The panels of this test article will be arranged in series, using the first three cartridges as pre-heaters for the final test section. This assembly will be mounted on a simple frame, and angled toward the heliostat field. Thermal input to the pre-heater cartridges and the test article will be performed by adding and subtracting mirrors as required, using inlet and outlet fluid temperatures as control parameters. Apart from the inlet sCO_2 control valve, no other control is necessary, though a valved bypass leg may be considered for additional control.

In one concept (see Figure 10) sCO_2 will be discharged from a pressurized reservoir at ambient temperature to a pump. The gas will be pressurized to the required level, then passed to the inlet of the first panel cartridge and brought to temperature as it passes through each subsequent cartridge. This design is an open loop with heated CO_2 vented to atmosphere. Test durations would be limited by reservoir capacity.

A secondary concept is the closed loop recirculating scheme depicted in Figure 11. In this arrangement the test section discharge flow rejects its heat via a heat exchanger to a cooling loop. The gas is then returned to the test section inlet. While this arrangement runs continuously, it entails a heat exchanger capable of sustaining high pressures and temperatures, which may be a substantial capital cost.

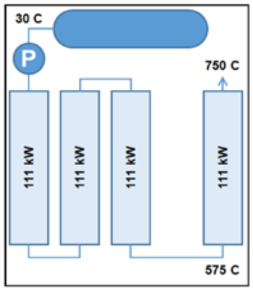

Figure 10 – Blowdown sCO_2 on-sun test schematic.

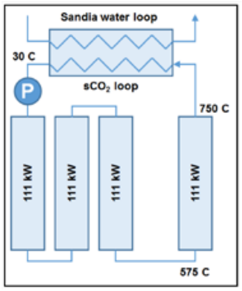

Figure 11 – Recirculating sCO_2 on-sun test schematic.

Recent discussions with Sandia have indicated that a recirculating sCO_2 loop (similar to that shown in Figure 41) may soon be installed there as part of their regular testing capabilities. In that case the cost and complexity of the testing task is greatly reduced. Brayton and its industrial partner would only be responsible for the test section and appropriate instrumentation; the test loop side would then be the responsibility of Sandia. Note that the proposed maximum sCO_2 flow rate and heat rejection capacity being considered are more than adequate for the needs of this program.

The target panel may be tested at any suitable small solar field, such as the Sandia National Solar Thermal Test Facility (NSTTF). This is currently the leading candidate site. Planning activities in the program focused on the NSTTF solar field, as Brayton is familiar with the limitations, infrastructure, and optical performance of that test bed.

A series of tests could explore both performance and durability of the test article:

- Design Point performance testing: With flux/power input well-characterized by water calorimeter and/or photo-thermometry, test panel at design point inlet temperature and flux conditions to achieve full temperature lift at or below predicted pressure drop (measure inlet and outlet conditions of HTF.) Attempt to accurately measure the panel metal temperatures, and characterize the absorber efficiency.
- Off-design performance testing: For a series of high and low power/flux cases, characterize the heat transfer and pressure drop performance at low and high power input and flow. Attempt to accurately measure the panel metal temperatures.
- Strain-management verification: Throughout testing, verify that the structural scheme (fixity, manifolds, strain-relief) is sufficient and effective.
- Controlled destructive testing: If a sufficient number of test articles are available, and time and budget allow, subject panels to accelerated damage conditions through excessive temperatures, locally high flux spots, pressure cycling, flux cycling, and other means to verify and explore material damage and failure mechanisms
- Quartz window testing: Perform some subset of tests with and without the quartz window, in order to characterize behavior and performance.

sCO_2 vs. Molten Salt Receiver Study.

The relative merits of supercritical CO_2 and molten salt as heat transfer media were investigated, considering temperature and thermal flux capacities and limitations, piping costs and ancillary issues. Of principal interest was the trade between extended operation but the lower temperature and efficiency of a molten salt based receiver, and the higher efficiency but more structurally challenged sCO_2 based variant. Ancillary issues such as maintaining salt temperature above the melting point were also considered.

A model was developed that performed a series of calculation to optimize the cost of the sCO_2 piping configuration for a given set of fluid flow conditions and performance requirements. The model uses an iterative Newton-Raphson multivariate solver to:

- Vary the number of parallel runs of pipe used to convey the sCO_2 in each direction
- Calculate the required flow diameter for the specified pressure drop
- Calculate the convective heat transfer coefficient between the fluid and the insulation (conservatively assuming a flow liner thermal resistance of zero)
- Vary the insulation thickness
- Determine the total heat transfer through the system and the resulting material temperatures
- Use temperature-dependent material properties for several candidate alloys to calculate the requisite pipe wall thickness needed at the derived pipe diameter in order to provide a 90,000 hour creep life

The results of this model were compelling. The least-expensive configuration consisted of single risers and down-comers, with both flows thermally insulated from a lower cost alloy pressure boundary. On the basis of this optimization, the calculated cost of the high pressure tower piping was \$18.60/kW_{th} for a 120 MW_{th} system. For comparison, the total piping cost for a molten salt system, based on the estimate of Sargent & Lundy[iv], was about \$12.92/kW_{th}. These results indicate that the direct sCO_2 receiver system – without the benefit of significant design optimization or sourcing investigations, has a capital cost approximate with that of the molten salt system. Furthermore, the additional operating cost benefits (both in terms of pumping and heating parasitics, as well as direct cycle efficiency implications) would only serve to further improve the LCOE of the direct sCO_2 receiver system, in all likelihood below that of the comparable molten salt receiver system.

Commercialization Plan

Brayton has worked within industry circles to find a company receptive to commercializing a CSP sCO_2 system. To that end, a business case has been proposed to two qualified commercialization partners; General Electric and Abengoa. These entities were the obvious choices as they have active programs to pursue sCO_2 power plant development. GE has a strategic relationship with eSolar, and are developing the core sCO_2 engine. Abengoa is an industry leader in the design and construction of CSP central receiver power plants, and has a strategic relationship with EcoGen for the solarized sCO_2 engine. Neither firm has active receiver development initiatives or is aligned with a solar receiver provider.

Brayton has also spoken with Rolls Royce, SASOL, Net Power, and Aerojet Rocketdyne, all Brayton clients working in this general area. Though Rolls, Rocketdyne, & Net Power are performing sCO_2 power generation research, their focus is not on solar applications at this time. Sasol, a South African company, performed exploratory studies but has expressed no intent to proceed at present.

The business case proposed by Brayton Energy to prospective partners incorporates the following general principles:

- Brayton Energy, an engineering firm with significant experience designing, fabricating, and testing solar receivers, has developed intellectual property associated with a cost-competitive, solar receiver for sCO_2 power generation.
- Brayton Energy wishes to ally with a commercialization partner to expedite the qualification testing and eventual commercialization of a sCO_2 power plant operable on concentrated solar power.
- The cost to perform qualification tests for said solar receiver technology will require approximately \$800,000 to \$1,200,000, depending upon a partner's support level on the mirror field characterization and on-site facilities.
- The cost to deploy the first commercial-scale, production prototype is estimated to be nominally \$350/kW_{th}, dependent upon the scale and site engineering and logistics. (\$148/kW_{th} for subsequent mature production)

Major Results

This section focuses on the current state of the sCO_2 receiver technology at the completion of the program. Specifically, this section will detail the absorber cell architecture, the component testing used to validate the performance and life of the cell design, layout and analysis of the full receiver, the manufacturing process developed to produce the receiver, experimental validation of Brayton's quartz tube window, and the overall receiver cost.

Cell Architecture

This program has developed a novel compact CSP absorber cell capable of operating at internal pressures and temperatures appropriate to the most efficient sCO_2 power conversion systems presently being designed. The cell features a dense matrix of extended heat transfer surfaces in the form of densely-packed folded fins brazed within an external shell. Fins not only enhance the heat transfer and provide excellent thermal communication between the external cell surface and the internal working fluid, but they also provide a distributed array of tensile cross-members to react high internal pressures.

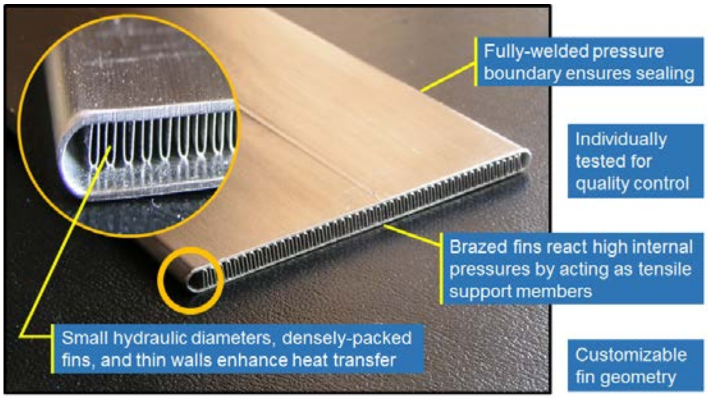

Figure 12 – The basic Brayton Energy sCO_2 solar absorber panel architecture, showing the hermetic boundary surface encapsulating high-density folded fin heat transfer surfaces that also provides tensile structural support to react the high-pressure working fluid.

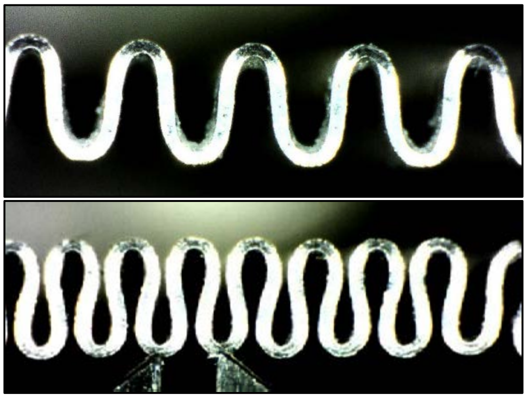

Figure 13 – Geometric comparison between as-folded fin (top) and compacted fin (bottom), in which the straight lines of the fin edges are deformed and curved fin edges result.

There is a high degree of geometric flexibility in the design of the cell, allowing its specifications to be tailored to meet required operating conditions. Fin densities in excess of 32 fin/cm (80fin/inch) can be produced in stainless steels and nickel alloys to meet full powerplant lives at the most extreme temperature and pressures being considered by sCO_2 power conversion equipment designers.

Component Testing

All components which comprise the construction of the heat exchanger cell architecture (shown in Figure 14) have been subjected to various tests to evaluate thermo-fluid and structural performance. The component areas of focus and subsequent test(s) include:

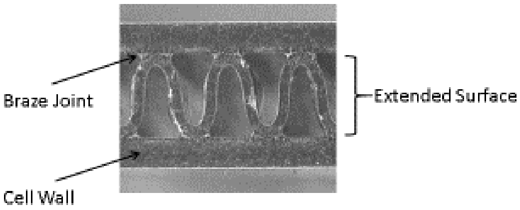

Figure 14 – Cross section view of typical heat exchanger cell construction.

Table 6 – Overview of component testing used to validate the performance and life of the absorber cell architecture.

DESCRIPTION	TEST	SUBTASK
Surface Performance Characterization	f & j Characterization Test	1.4.2
Fatigue Performance	High Temperature/Pressure Low Cycle Fatigue Test	1.4.3
Braze Joint/Structural Performance	Cold Burst Test, Creep Test	1.4.4

Surface Performance Characterization

Brayton successfully commissioned a heat transfer surface performance characterization test station (Sub-Task 1.4.1) and tested multiple surfaces currently being employed in high-pressure sCO_2 heat transfer applications. The general test operational schematic is shown in Figure 15. Images of the completed unit in during test are can be seen in Figure 16 and Figure 17.

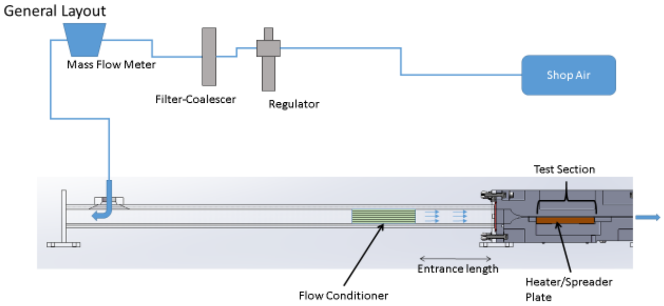

Figure 15 – Schematic of Surface Characterization Test Station.

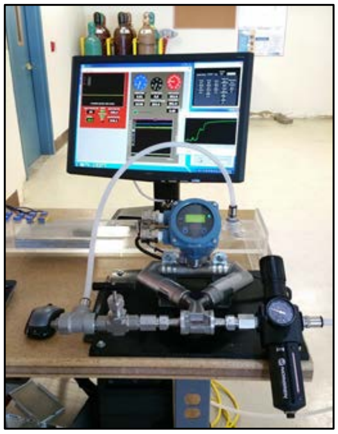

Figure 16 – Test setup for the heat transfer surface performance characterization rig.

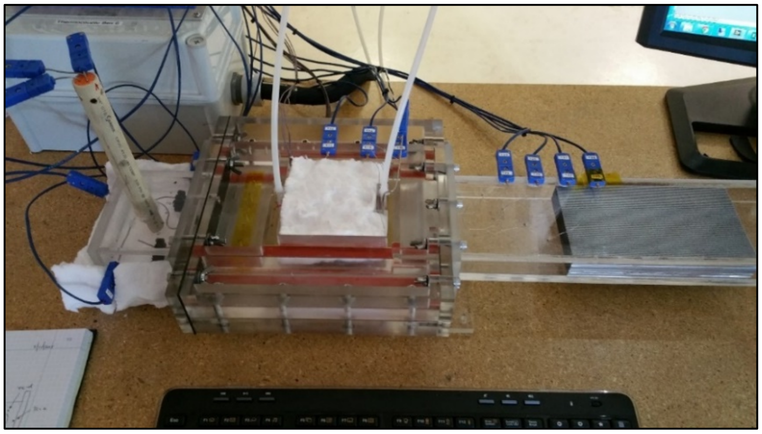

Figure 17 – Test setup for the heat transfer surface performance characterization rig. A section of the heat transfer surface can be seen as the metallic block to the right, housed within a clear acrylic flow duct.

Theory

The test apparatus is designed to measure relevant fluid temperature and pressure across a given surface specimen housed within the test section. During test, a fixed mass flow is prescribed while a fixed heat flux is applied to the crests of the extended surface under test as shown in Figure 18. Static pressure measurements are made at the Inlet and Outlet of the test section.

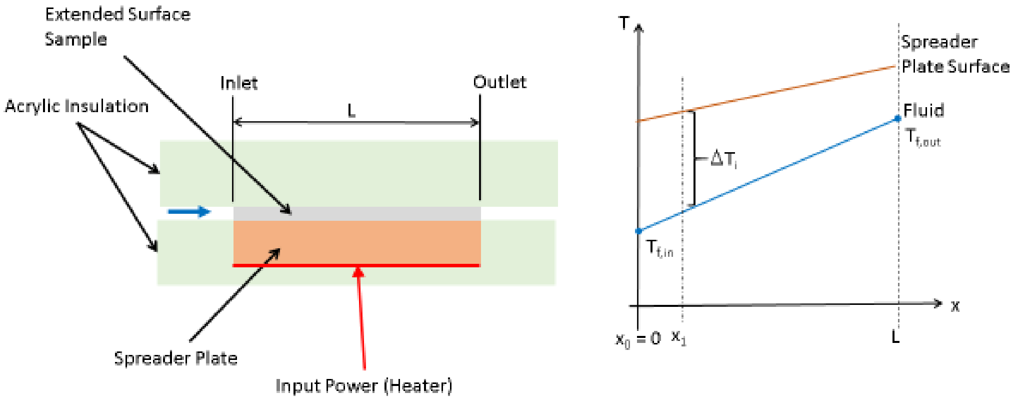

Figure 18 – General operational scheme describing surface characterization testing.

The outside of the test section is heavily insulated and maximum channel height is 3 mm. It is assumed that variations in pressure and temperature occur only along the axis of flow. Thermocouples immediately below the surface of the Spreader Plate provide an accurate survey wall surface temperature along the axis of flow. The flow control volume is discretized along the flow length and an average overall heat transfer coefficient is developed using,

$$UA = \frac{1}{N}\sum_{i}^{N} UA_i = \frac{\Delta T_i}{q_i} \tag{1}$$

Using the result from (1) the Colburn Modulus is generated and used as the metric for thermal performance,

$$j = \frac{Nu}{Re \cdot Pr^{1/3}} \tag{2}$$

Using the standard definition of friction loss within the surface matrix the Fanning friction factor is determined using the measured differential pressure and mass flow,

$$f_{fanning} = \frac{\Delta P D_H}{2 l \rho U^2} \tag{3}$$

where the average density and bulk velocity are employed.

During testing each trial surface is subjected to a specific mass flow (Re) and heat flux. Steady state data is recorded and a new set of test conditions applied. The final set of f & j data accurately describes thermo-hydraulic characteristics for a specific surface geometry.

Results

The matrix of surfaces tested is shown in Table 7 and includes variations with fin thicknesses, heights, and densities equivalent to those specified for the SunShot absorber cell architectures. Note that those samples with densely compacted fin sets (specifically Test ID #1 & 2) have physical geometries that are significantly different from as-folded geometries. This difference is clearly shown in Table 7.

Table 7 – Test matrix for Surface Characterization testing.

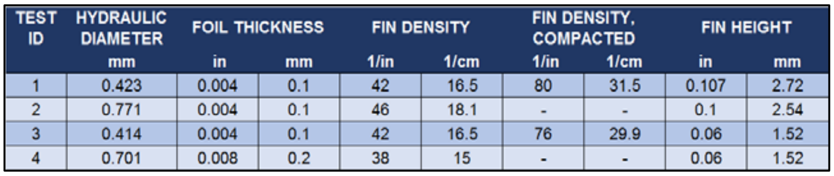

TEST ID	HYDRAULIC DIAMETER	FOIL THICKNESS		FIN DENSITY		FIN DENSITY, COMPACTED		FIN HEIGHT	
	mm	in	mm	1/in	1/cm	1/in	1/cm	in	mm
1	0.423	0.004	0.1	42	16.5	80	31.5	0.107	2.72
2	0.771	0.004	0.1	46	18.1	-	-	0.1	2.54
3	0.414	0.004	0.1	42	16.5	76	29.9	0.06	1.52
4	0.701	0.008	0.2	38	15	-	-	0.06	1.52

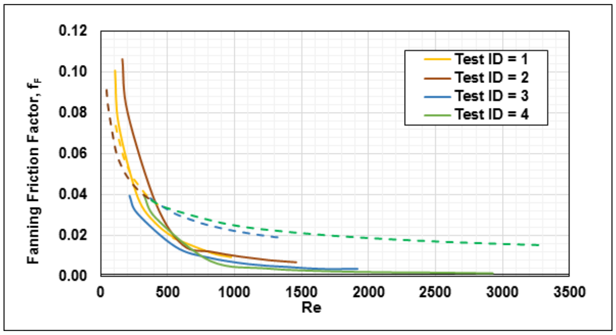

Figure 19 – Friction factor versus Re for test surfaces #1-4.

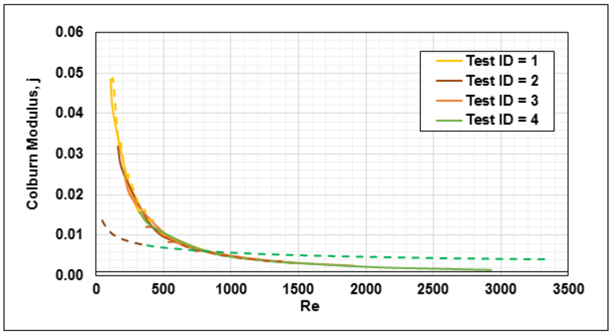

Figure 20 – Colburn Modulus vs. Re for test surfaces #1-4.

Fanning friction factors (f) and corresponding Colburn Moduli (j) for each surface are shown in Figure 19 and Figure 20 over a range of Reynolds numbers, including the range of interest for sCO_2 absorber designs. Note: corresponding numerically predicted results for each Test ID shown superimposed and denoted with dashed lines in same color.

Burst Strength Characterization

A number of braze alloys were investigated as candidates for internal cell bonding. The list of candidate alloys with element concentrations is shown in Table 8.

Table 8 – Table of candidate braze alloys.

														Braze Cycle Temperature		
MANUFACTURER /VENDOR	*PRODUCT*	*CONFIGURATION*	*%NI*	*%CR*	*%SI*	*%P*	*%B*	*%FE*	*%MO*	*%C*	*SOLIDUS $^oC(^oF)$*	*LIQUIDUS $^oC(^oF)$*	*BRAZE T $^oC(^oF)$*	^{o}F	^{o}C	ΔT over T_{liq} (^{o}F)
Wall Colmonoy	NB-30	Powder, paste	Balance	19	10.2					0.06	1080 (1975)	1135 (2075)	1177 (2150)	2185	1196	110
Wall Colmonay	NB-150	Powder, paste	Balance	15			3.5			0.06	1055(1930)	1055(1930)	1065 (1950)	2012	1100	82
Metglas	MBF-53	Foil, 0.0015" Thk	Balance	15	7.3		1.4		5	0.06	1045 (1900)	1127 (2060)	1195 (2183)	2185	1196	25
Metglas	MBF-53	Foil, 0.0012" Thk	Balance	15	7.3		1.4		5	0.06	1045 (1900)	1127 (2060)	1195 (2183)	2185	1196	25
Metglas	MBF-50	Foil, 0.0015" Thk	Balance	19	7.3		1.5			0.08	1052 (1924)	1144 (2091)	1170 (2138)	2185	1196	25

Both powder and foil type braze alloys were included for tests:

- NicroBraz (NB) – Powder
- MetGlas Foil (MBF) – Foil

Cold burst tests were used to evaluate room temperature strength performance and define the optimal braze alloy and manufacturing parameters to be used for the receiver cell build process. Tests were conducted using open faced samples charged hydrostatically at room temperature until failure is achieved. A low charge rate of less than 50 psig/s is maintained thereby avoiding strain-rate effects not present in normal operation. Each test sample is comprised of 4" square layered geometry (see Figure 21) consisting of:

- Top/Bottom boundaries; 0.020" thickness
- Folded Fin; 0.060" height x 0.008" thickness x 38 fin/in
- Material: Inconel 625

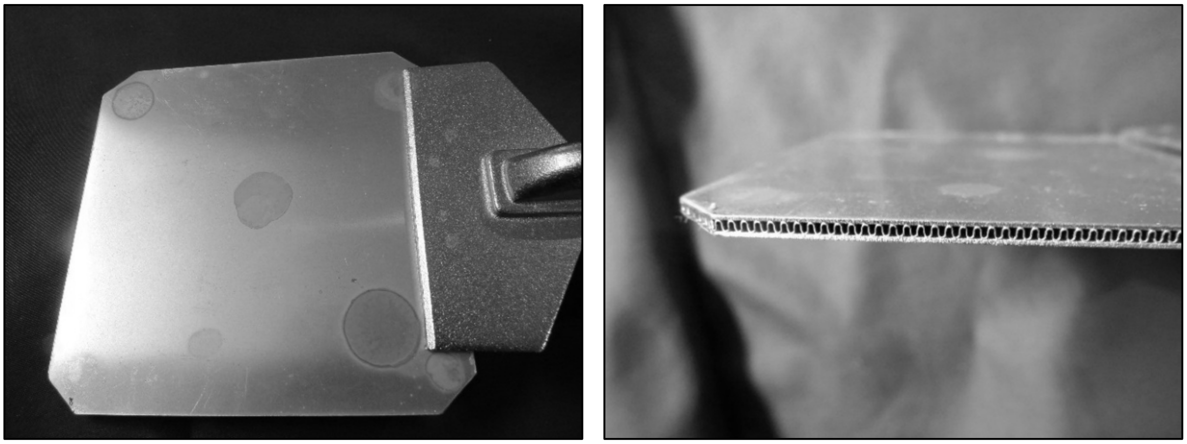

Figure 21 – Example of 4" x 4" test sample for use in Cold Burst Testing.

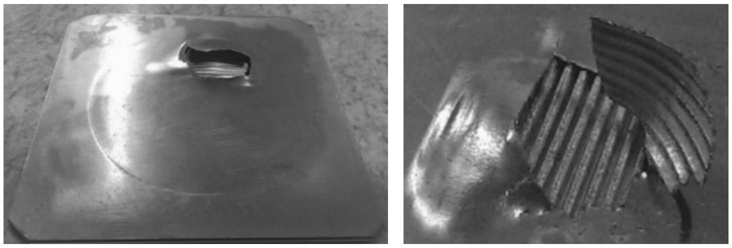

Figure 22 – Example of typical failure mode from Cold Burst Tests.

Table 9 – Average cold burst test data (*Average of highest data values, no failure reported).

AVG. BURST PRESSURE (MPa)	
Braze Alloy	*Parent Metal-IN625*
MBF53, 0.0015" THK	87
NB30	81
MBF53, 0.0012" THK	76
MBF50, 0.0015" THK	62

All bursts occur as a result of localized tearing of the fin from the wall due to braze joint rupture. Once the integrity of this bond is violated the wall begins to delaminate as the unsupported area increases, ultimately resulting in the rupture of the wall material (example shown in Figure 22).

Results

Averaged burst pressure data is presented in Table 9. The foil type braze alloy MBF53, (0.0015" thick foil) was selected as the optimum candidate for fin/wall brazing. In addition to exhibiting excellent strength characteristics the foil construction allows for fast, repeatable installation during assembly.

Micrographic analysis reveals the local delamination is contained within the braze joint with little to no parent metal involved as shown in Figure 23. Figure 24 depicts a typical brazed joint using MBF53 type braze alloy with IN625 material. Micrographic evaluation of show high quality, consistent braze fillet radius to fin thickness ratio, r_b/δ =0.5 using current process methods.

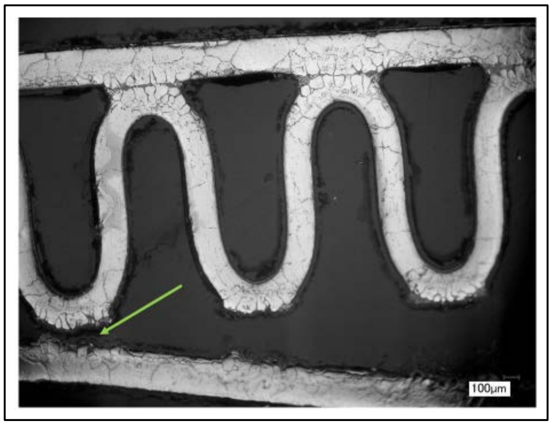

Figure 23 – 100x Close up view of braze joint rupture.

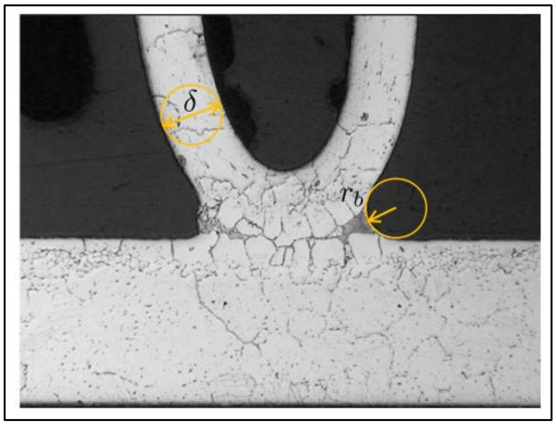

Figure 24 – 50x Micrograph of MBF53 braze joint with IN625.

FEA investigation of the braze joint depicted in Figure 24 reveals significant concentrated stress occurring within the fillet as a result of the tensile and moment forces. As a result, this characteristic failure mode corresponds with FEA predictions.

Fatigue Testing

The following section describes the relevant stress models used to simulate stress fields, their variation with Creep and their application to Fatigue.

The equivalent stress evaluated across the mid-plane of the internal structure, being in the load path and principally tensile is considered the far-field stress relevant to internal pressure loading.

The following relation is developed by examining the force balance between internal pressure supported per fin.

$$\sigma_{mp} = \left[\left(\frac{1}{\delta \cdot f_{pu}} - 1 \right) + \theta \right] \cdot p_i \tag{4}$$

where δ, f_{pu} and p_i denote fin thickness, fin density (fins per unit length) and internal pressure respectively. The Θ term is included to account for increased surface area for the terminal fin and is zero for inboard fins.

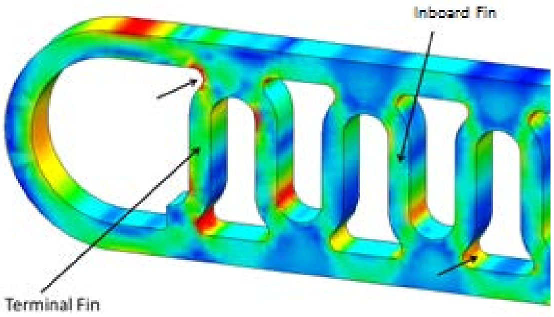

Figure 25 – Example FEA stress map for folded fin showing concentration within braze fillets (black arrows).

Through detailed FEA the characteristic stress distribution for both the inboard and terminal fins have been investigated (see Figure 25). Results were used to develop models describing stress concentration factors to account for elevated stress levels occurring within the braze fillet as a function of the mid-plane far-field stress.

Two stresses of interest occur at the braze joint; peak stress and average section stress. The peak stress (denoted with point A in Figure 27) represents the maximum stress occurring at the braze joint fillet surface. Stress at this location is determinate of crack initiation during cyclical loading and is depicted on standard Low Cycle Fatigue (S-N) curves. The average section stress denotes the averaged stress across the section denoted by AB in Figure 27. This section is determinate of creep life for a given alloy and temperature history. The corresponding concentration factors and are defined as,

- k_t': Peak surface stress concentration factor
- $\overline{k_t}$: Average section stress concentration factor

Both terms exhibit logarithmic trends overtime as shown in Figure 26.

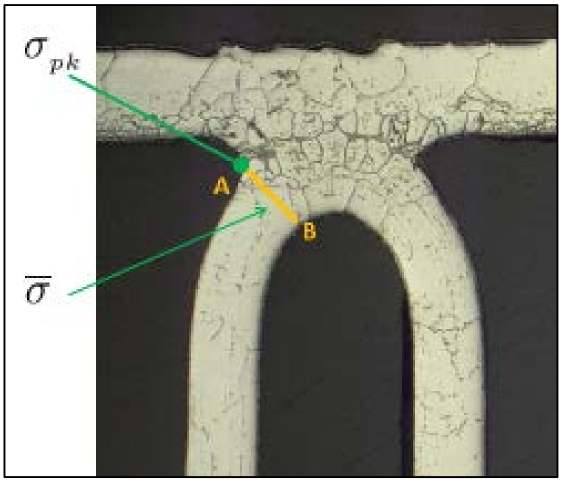

Figure 26 – Image of braze joint depicting location of peak and section stress.

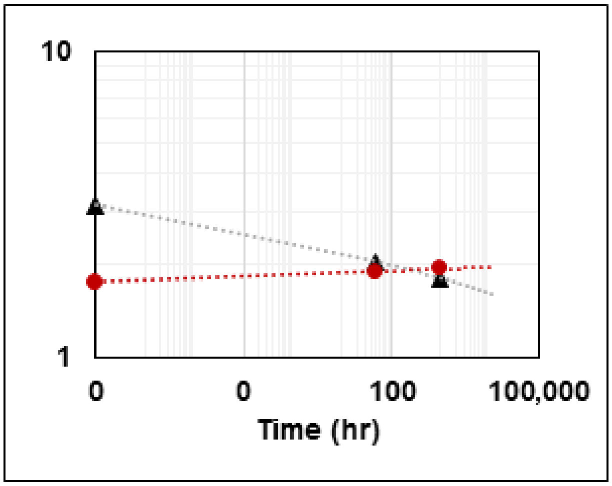

Figure 27 – Graph of stress concentration factors for peak and average section stress.

The resulting general expression is used to describe the design life for a particular finned geometry, in terms of fatigue and creep respectively is then,

$$\sigma' = k_t' \cdot \sigma_{mp} \tag{5}$$

$$\bar{\sigma} = \bar{k}_t \cdot \sigma_{mp} \tag{6}$$

where the appropriate mid-plane (far-field) stress is determined from (4).

Test Panel

To generate representative test data, a Test Panel has been designed to accurately capture the full scale receiver cell architecture (refer to Figure 14) and manufacturing process. Straight, folded-fin serves as the extended surface and is brazed in to the inside walls to create the internal heat exchange surface as shown in Figure 14. The formed shells which comprise the walls are welded along raised seams to complete the pressure boundary.

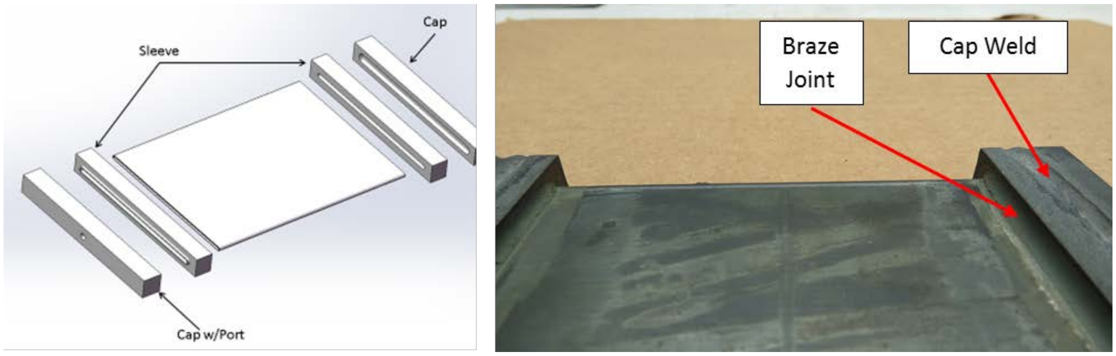

Figure 28 – Test panel model (a) depicting components and (b) completed unit.

A welded/brazed Cap & Sleeve configuration (see Figure 29) is used to effectively seal and support the cell ends while the unit is pressurized. In addition to providing a hermetic seal, the secondary brazing process strengthens the original fin-wall braze joint due to the extra diffusion dwell during brazing.

The processing parameters and braze alloy specifications have been judiciously refined using extensive feedback from data collected during testing. The result is a truly optimized build process with high yield rates while exhibiting excellent strength characteristics.

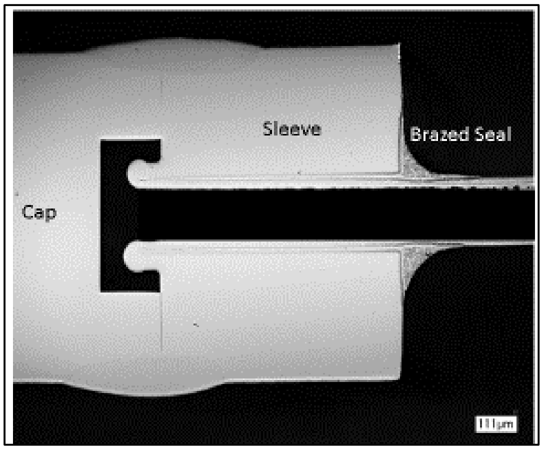

Figure 29 – Cross section showing cell bonded to Cap & Sleeve.

Theory

Fatigue strength of candidate Heat Exchanger architecture is governed by the localized stress concentration occurring at the terminal braze joint as discussed earlier. Because this stress diminishes to a near steady value with creep relaxation over a small fraction of the receiver lifetime, samples are subject to steady creep for 2 hours prior to pressure cycling (refer to Figure 30). The result is a “relaxed” stress field within the braze fillet for a given applied internal pressure.

The general mission profile for fatigue testing is shown in Figure 30. The green line is shows the reduction of peak stress during the creep stress portion. Once the prescribed relaxation period is achieved the cyclic loading is applied to the test specimen.

The resulting data output is represented using typical Stress versus Cycles (S-N) graphs. Standard Least-Squares regression analysis are applied to the data set to develop Low-Cycle Fatigue (LCF) correlation used to predict structural lifing bounds.

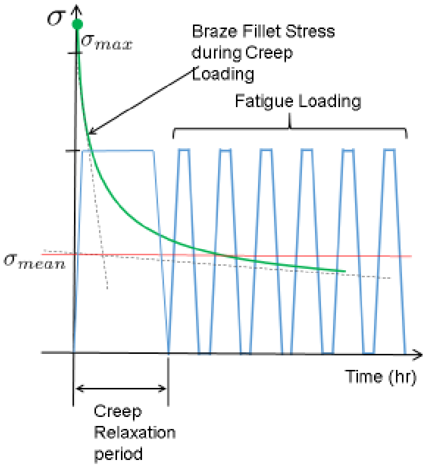

Figure 30 – General mission profile for fatigue test.

Test Rig

Tests are performed using Brayton Energy's Fatigue Test Station pictured below in Figure 31. The unit is capable of charging a single Test Panel up to 10,000 psig (69 MPa) using CO_2 as the working fluid. The test furnace is capable of steady state temperatures up to 1100^{o}C. During tests, Test Panels are exposed to high temperature while simultaneously subjected to cyclic charge/discharge pressure loading. Tests continue until rupture is achieved. Cycles and test duration are recorded.

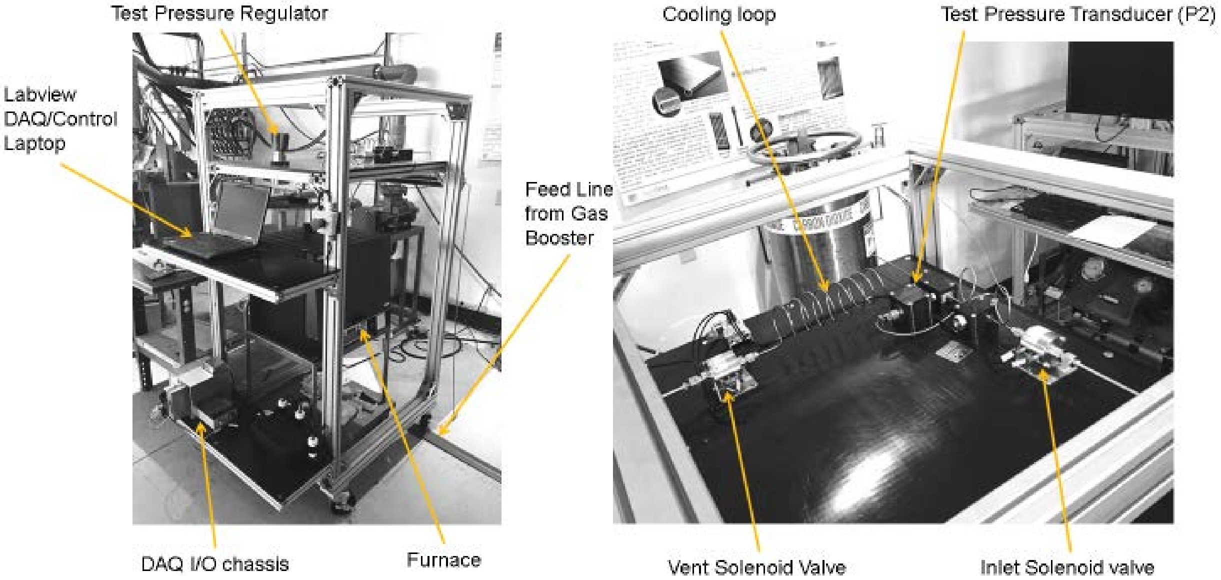

Figure 31 – Completed high temperature, high pressure Fatigue Test Station.

Table 10 – Test matrix for Low Cycle Fatigue tests.

ID	CYCLES TO FAILURE	TEST PRESSURE AND DWELL		TEST TEMPERATURE	CREEP RELAXATION PRESSURE AND		FIN THICKNESS	FIN HT	FPI	ALLOY
-		psig	sec.	C (F)	psig	hr	in	in	fin/in	-
1	464	6526	20	751 (1382)	5000	2	0.008	0.06	38	IN625
2	1,139	5000	20	752 (1382)	5000	2	0.008	0.06	38	IN625
3	11,189	4350	20	752 (1382)	5000	2	0.008	0.06	38	IN625
4	801	6526	20	752 (1382)	5000	2	0.008	0.06	38	IN625

Results

To date four test panels have been tested; details of the test conditions are outlined in Table 10 Results are used to generate the corresponding S-N curve – shown as the blue data in Figure 32 – demonstrate cyclic life is well in excess of the target (shown in red). For reference, manufacturer-supplied curves for annealed bar samples (green data) are shown for two different temperatures.

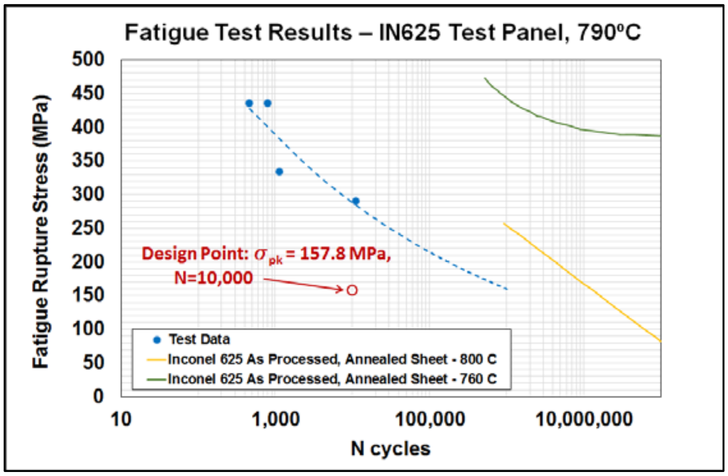

Figure 32 – Results for Low Cycle Fatigue tests.

Using results from testing and the relation in (6), a minimum fin density can be calculated as a function of fin height, thickness and design stress (40 ksi based on results) – see Table 11. An example Design Point – defined in Table 12 – is graphed for reference.

The conclusion from these data is that the panel assemblies, including the cell-to-header connections, meet the programmatic fatigue life goal. Note:

- Materials and configurations being evaluated in these tests correspond to selections being incorporated into the absorber design, as described in "Manifold Design". As such fatigue test results are indicative of as-manufactured absorber structures.
- Preliminary cycle specifications from General Electric are considerably lower than those represented in these fatigue tests. This suggests that results are conservative for the proposed application.

Table 11 – Minimum fin density required to meet fatigue life requirements.

Fin Height mm (in)	Fin Thickness 0.152 mm (0.006")	Fin Thickness 0.203 mm (0.008")
1.0 (0.040")	46	31
1.5 (0.060")	60	37
2.0 (0.080")	86	45

Table 12 – An example design point, corresponding to the one shown in Figure 32.

EXAMPLE DESIGN POINT	UNITS	VALUE
N cycles	-	10000
Pressure	MPa	27.7
	ksi	4.017
Fin Thickness	in	0.008
Fin Height	in	0.06
Fin Density	fin/in	50
Mid-Plane Stress		13.559
Peak Stress Concentration Factor		2.326
Peak Stress	ksi	31.54

Creep Testing

The equivalent stress model described above in the Fatigue Testing section also applies to creep testing and analysis. The test sections described in the Fatigue Testing section are identical to those used in creep testing.

Theory

Creep behavior of metals is time-dependent non-elastic deformation of the material due to tensile or compressive loading occurring at elevated temperature. As a guideline 40% of the melting temperature of an alloy may be used as a temperature threshold, above which creep should be considered. The general temporal relation describing the material strain rate is depicted in Figure 33. Stage I represents the

Primary creep segment during which rapid grain boundary dislocation occurs. This initial creep set is then followed by a period of steady state creep during Stage II characterized by constant strain rate. Finally, during Stage III, the cross sectional area decreases to a point where creep accelerates and rupture occurs.

Rather than performing traditional tests to develop creep characteristics of a particular material, a plate-fin panel is used as the test specimen. This construction captures all material, geometric, processing and loading variables associated with the heat exchanger cell.

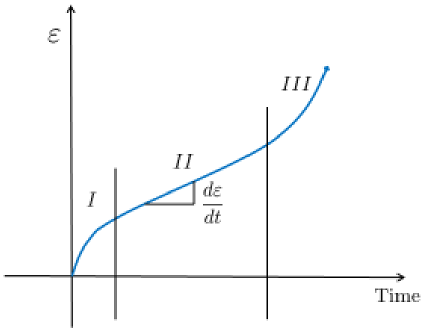

Figure 33 – Example curve showing three stages of strain during Creep.

Time-to rupture is be recorded for samples subjected to a range of temperature-pressure exposures. Given the creep-life specification of 100,000 h, testing is accelerated with temperatures and/or pressures in excess of operating conditions. Larson-Miller parameter LMP, shown here is used to plot and extrapolate measured data.

$$LMP = T\,[C + \log(t)] \tag{7}$$

Using this relation, it can be shown that[v] a general form of the relation describing creep rupture stress as a function of rupture time and temperature is written as,

$$\log(\sigma_r) = \beta_1 \log(t_r) + \beta_2 \tag{8}$$

Test Rig

The Test Panel was subjected to high temperature/pressure loading to induce material creep. Tests were run until rupture and the corresponding duration recorded. This data was used to develop the Larson-Miller type rupture time vs. stress parametric relation used to predict structural lifing bounds.

Testing was performed using Brayton Energy's Creep Test Station pictured below in Figure 34. This unit has been designed and built to charge up to five Test Panels at pressures up to 15,000 psig (103 MPa) using CO_2 as the working fluid while subjected to steady state temperature up to 850°C.

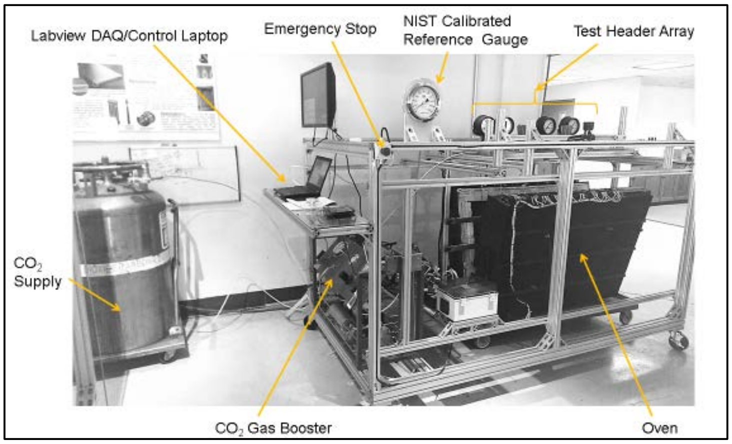

Figure 34 – Brayton Energy's Creep Test Station

The furnace is an insulated steel enclosure which is hinged along the bottom to allow access. The internal test volume is enclosed by 4" (min) of ceramic based insulation board. Two arrays of rod heaters (each rated at 800W) are installed symmetrically through the top face along the length of the cavity.

Significant effort was made to limit experimental error. The results of rigorous uncertainty analysis applied to the current test equipment yields the following error bounds for 95% confidence interval;

- Temperature: +/- 12.7 ^{0}C
- Pressure (gage): +/- <1 psi (6.9 kPa)
- Time: +/- 0.5 min

Table 13 – Creep test matrix.

ID	Rupture Time	Charge Pressure	Rupture Stress	Uncertainty
-	hr	MPa (ksi)	MPa (ksi)	MPa (ksi)
1	1076	22.06 (3.20)	174.65 (25.33)	3.8 (0.6)
2	533	40.25 (5.84)	317.43 (46.04)	6.9 (1.0)
3	103	47.20 (6.85)	368.61 (53.46)	8.0 (1.2)
4	36	53.00 (7.69)	411.31 (59.65)	9.0 (1.3)

Results

Creep rupture data have been generated at a test temperature of 735°C. This reference temperature was selected as it is expected to be the highest braze joint temperature, as predicted by solar simulations. See Table 13 for the corresponding test matrix. Results are plotted in Figure 35 along with a reference curve generated from published manufacturer's data for Alloy 625 annealed sheet at the test temperature of 735^{0}C. Results show good agreement between curves and indicate that the current manufacturing methods employed for receiver construction exhibit excellent braze joint efficiency resulting in near parent metal strength. Figure 36 presents data as a design selection tool for fin geometry required a given creep life.

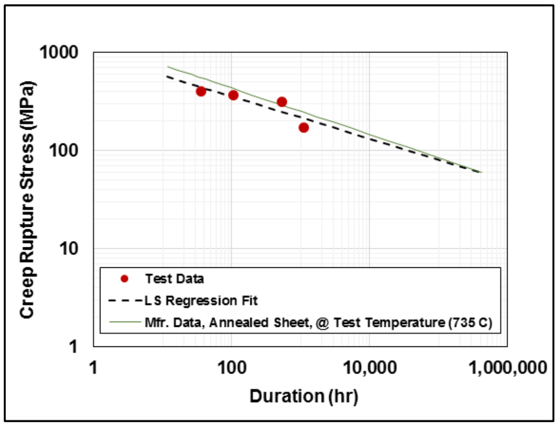

Figure 35 – Creep Rupture Stress vs. Dwell Time (IN625 Samples)

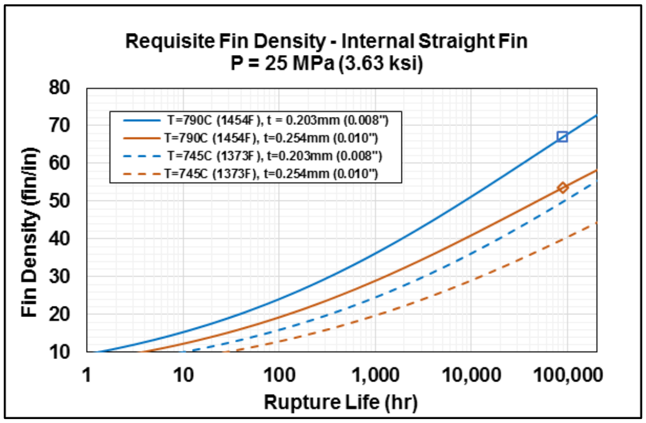

Figure 36 – Required fin density for a 90,000 hour creep life as a function of fin thickness and metal (IN625) temperature

Quartz Window Testing

The primary test objective is to directly measure the convective heat loss from the SunShot CSP receiver. With heat loss experimentally measured with and without the quartz tubes window, accurate heat loss models were created. These experimentally validated models enable better receiver optimization and cost analysis.

In previous SunShot phases, Brayton Energy designed a unique CSP receiver panel. This panel uses CO_2 as the heat transfer fluid, with quartz tubes between high pressure CO_2 cells to limit heat loss and increase absorption. To measure the effect of the quartz tubes and overall heat loss, a single panel with comparable geometries was constructed. The test panel was operated at the temperature expected in the receiver tower, with a mass flow chosen to yield a 90°C temperature drop.

The quartz tube array is intended to inhibit airflow across heated absorber cells, thereby decreasing convective heat loss. Without tubes, it is reasonable to expect vertical convection 'chimneys' of air current to form between and in front of the cells, lowering the panel's efficiency. These tubes also allow higher frequency solar radiation through, refracting it into the cells and increasing absorption, while blocking infrared radiation from escaping the panel. Radiative capture is thereby improved, while loss is reduced.

Test Panel

To gather heat loss data a test panel was constructed and tested under a variety of configurations. On the central receiver tower, CO_2 enters through the middle of the panel and is conveyed up and down through vertical cells while being heated. The greatest temperatures are therefore at the top and bottom of the panel where CO2 is in its fully heated state. Inversely. flowing the panel in reverse hot air input will yield the same temperature distribution, so will give the best heat loss data. A diagram of the panel and test conditions is shown in Figure 37.

The panel was constructed as shown in Figure 38 below. Air was used as the working fluid, passing through pieces of readymade, rectangular carbon steel piping, two of which made up each cell. This made running the experiment much cheaper and easier, while still allowing the panel to work at the desired temperature and mass flow. Quartz tubes were inserted as shown in Figure 39, with smaller tubes sitting on top of the cells, nested between the larger tubes.

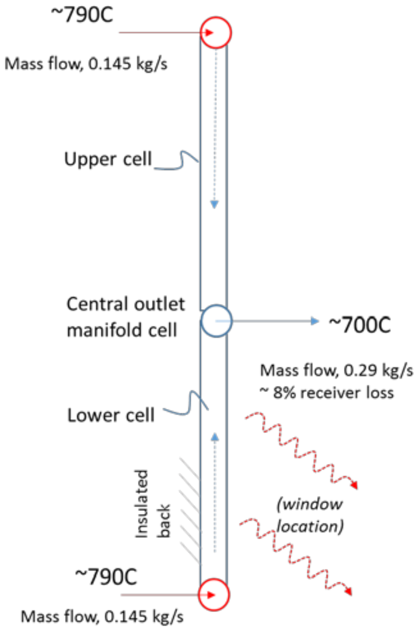

Figure 37 – Schematic of the quartz window test section, with conditions.

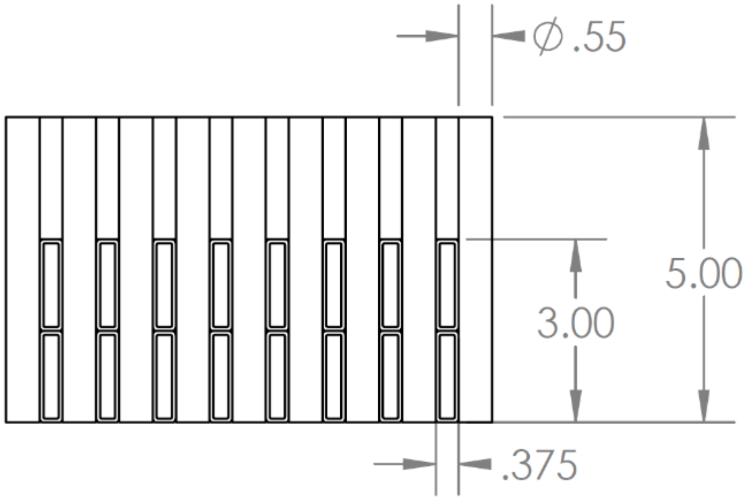

Figure 38 – Detail of the quartz window test section absorber cells

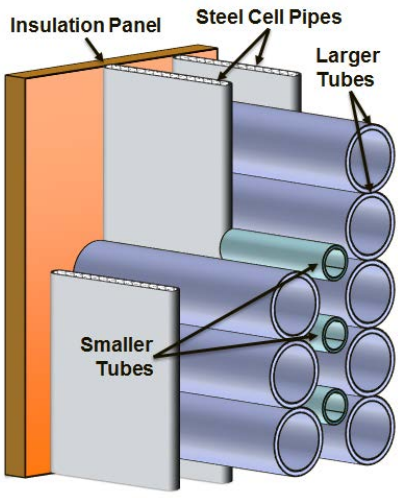

Figure 39 – Schematic of the quartz tube window test section configuration.

The Panel consists of sixteen cells, eight above and eight below the center manifold. These are welded to intake manifolds at the top and bottom, and backed with insulation board and steel framing. A diagram of the full panel (without steel framing) is shown in Figure 40. It includes only one row of each size quartz tube for clarity. Figure 41 and Figure 42 show the actual completed test section in the lab, including the quartz tube window.

The larger quartz tubes are attached directly to the insulation board using Sodium Silicate 40% (water glass). The smaller ones are sewn together using stainless steel wire and attached to small steel pegs welded onto the cells. These methods were reasonably simple and cost effective, but may not be suitably rugged for a protracted test or commercial system. Potential tube attachment techniques for long-term use are described in the conclusions section.

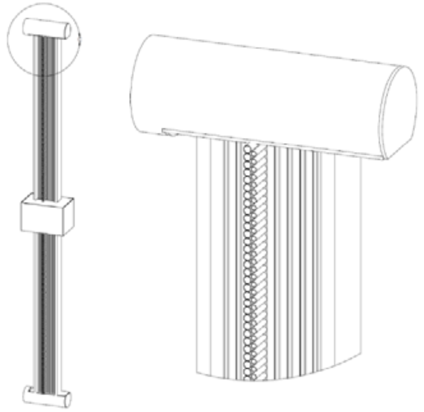

Figure 40 – Schematic of full quartz window test section panel

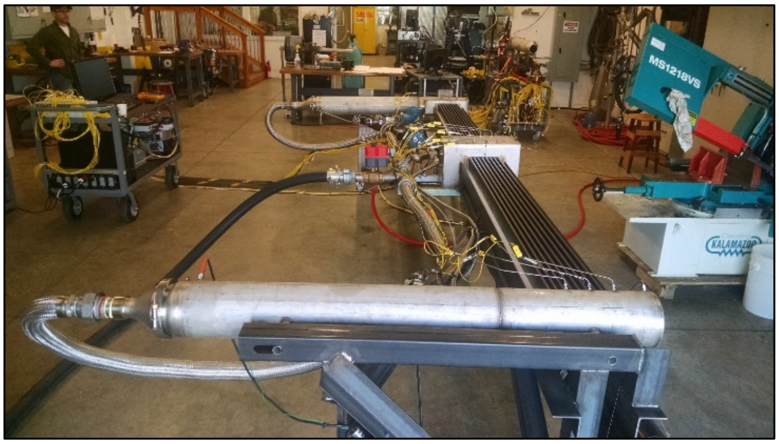

Figure 41 – Picture of completed quartz window test section

Figure 42 – Picture of quartz tube window on test section

Table 14 – Design point operating conditions and dimensions for a baseline receiver panel and the quartz window test panel.

PARAMETER	UNITS	RECEIVER PANEL	TEST PANEL (EXPECTED)
Temperature hot	°C	715	790
Temperature cold	°C	546	700
Cell length	m	1.82	1.82
Cell width	mm	6.350	9.525
Cell gap	m	0.014	0.014
Working fluid	-	CO_2	air
Mass flow per cell	kg/s	0.108	0.0181
Inlet pressure	kPa	25,000	12.9

A table of the test conditions is shown in Table 14. Mass flow was chosen to yield a 90C temperature drop for an estimated 92% efficiency. For this receiver configuration, we expect the power per cell to be 24.6 kW. This puts the estimated 8% power loss per cell at 2.0 kW. Solving $q = \dot{m}\, Cp_{air}\, dT$ for $\dot{m}$, mass flow per cell was determined to be 0.0181 kg/s. Using the pipe geometries specified above the pressure drop through the cells was modeled. Assuming the outlet pressure is ambient, an inlet pressure of 12.9 kPa is required.

Data Collection

The panel was assembled and tested in the horizontal position. At this orientation, heat loss is expected to be almost entirely due to outward radiation. This assumption allows us to see the radiation blocking effect of the quartz by running the panel with and without tubes. Orientations and configurations tested include:

- Horizontal panel without any quartz tubes

- Horizontal panel with both tall quartz tubes and cell-top quartz tubes
- Vertical panel, raised 20ft above the ground with no quartz tubes
- Vertical panel, raised 20ft above the ground with all quartz tubes

A diagram of the vertical test configuration is shown in Figure 43. Data was gathered at a number of different orientations and configurations. At each configuration, the setup was allowed to reach a steady state, then the following measurements were taken:

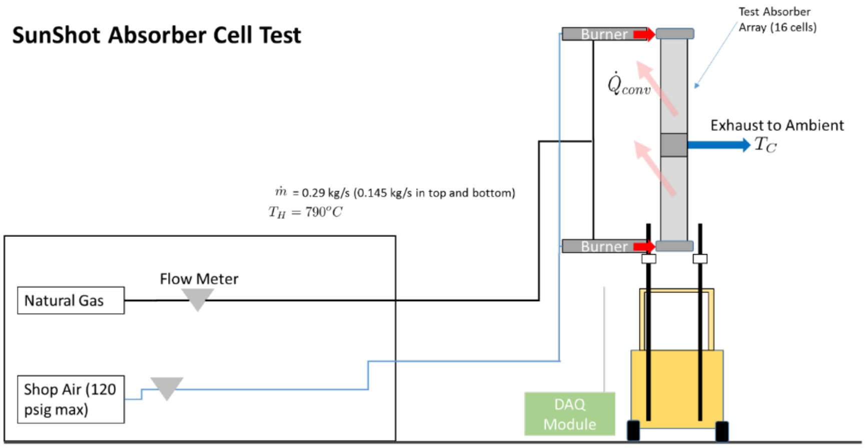

Figure 43 – Schematic of the quartz window test setup.

- Inlet and outlet air temperature using an array of thermocouples)
- Mass flow and heating fuel input (using Coriolis meters)
- Surface temperatures (using several thermocouples and a thermal camera)
- Outlet manifold pressure, pressure drop across the cells (using pressure gauges)
- Wind speed and direction (using an anemometer, for outdoor tests only)
- Air pressure data, taken from the National Weather Service

Raw Data

The theoretical heat loss due to radiation at room temperature is about 0.9 kW per cell. At the experimental mass flow this gives an outlet temperature drop of 42°C. Additional heat loss can be attributed to convection. The insertion of the radiation blocking quartz tubes reduced the required mass flow substantially. Nine cases were studied, and are described below.

Table 15 – Overview of the 9 quartz window test case conditions

PARAMETER	UNITS	CASE 1	CASE 2	CASE 3	CASE 4	CASE 5	CASE 6	CASE 7	CASE 8	CASE 9
Orientation	-	horizontal	vertical	vertical	vertical	vertical	horizontal	horizontal	vertical	vertical
Quartz Tubes	-	none	none	none	none	all	all	all	all	all
Avg. Wind Speed	m/s	0.00	4.60	2.90	3.80	2.44	0.00	0.00	1.61	3.38
Wind Direction*	-	0	0	0	45	90	0	0	0	45

* wind direction is measured in degrees from normal into panel face

Figure 44 – The quartz window test section during the day, elevated to enable the establishment of free field natural convection currents. Two absorber panels are situated one atop the other with a central manifold between them.

Figure 45 – The quartz window test section operating at night. Note the desired temperature gradient – wherein the peak temperatures are at the top and bottom manifolds – may be seen clearly.

For each test the top and bottom burners were tuned to yield the same inlet temperatures. These temperatures were increased to 790°C, and maintained while the panel heated and the outlet temperature steadied. Figure 46 illustrates a standard data run. The steady state heat loss results from each test are shown in Figure 47.

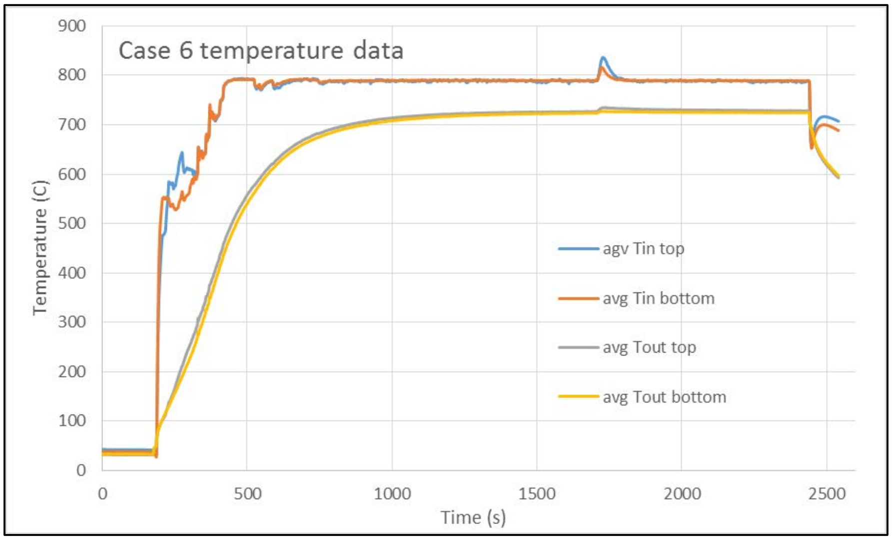

Figure 46 – Typical quartz window data run, showing flow inlet and outlet temperatures into each of the two panels.

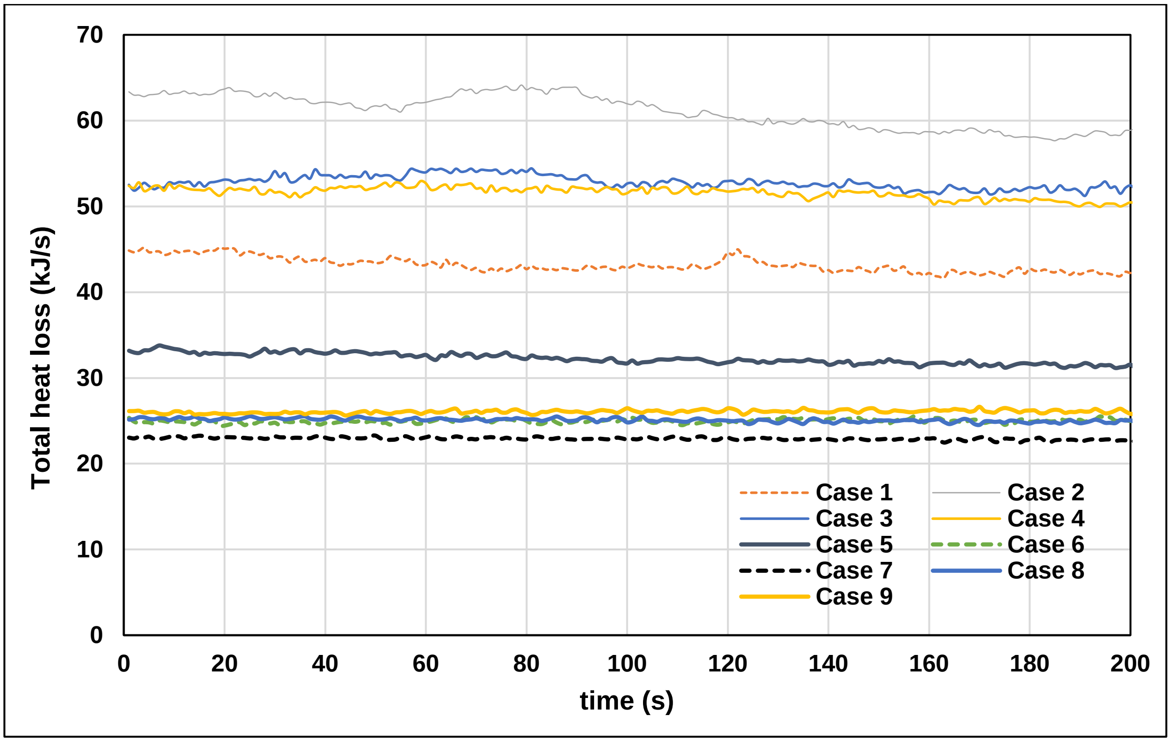

Figure 47 – Steady state raw data heat loss trends for each of the 9 test cases. Note that there was no quartz window in place for tests #1-4, while the quartz window was in place for tests #5-9. A marked reduction in heat loss (combined radiation and convection) can be observed with the addition of the quartz tube window.

Several conclusions can be made from this, primarily that:

- The quartz tube window has a significant convection and radiation blocking effect in all orientations.
- The quartz tubes significantly reduce convective heat loss.
- Wind speed and direction have significant heat loss effects.

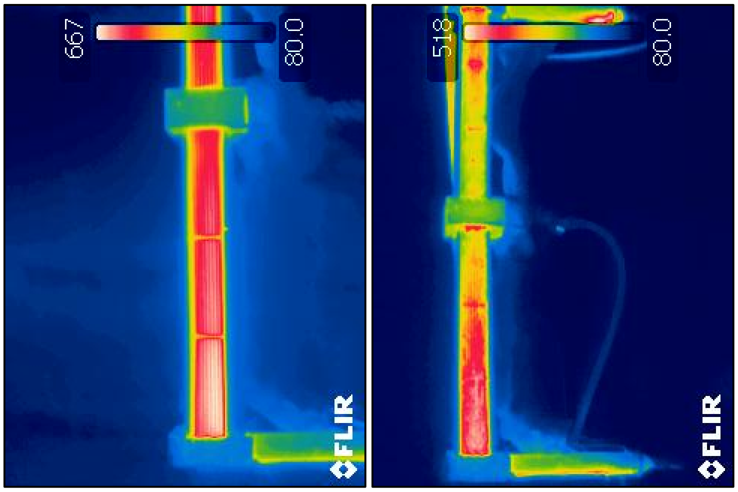

Figure 48 – Temperature profiles from vertical tests without (left) and with (right) quartz tubes.

The quartz window also created a very different temperature profile, as shown in the thermal images in Figure 48.

Even when running at the same inlet and outlet temperatures, the temperature distribution viewed through an infrared camera appears different. An analysis of the bottom right image in Figure 49 was used to find the window temperature, an essential metric for the heat loss model. This image captures the glass temperature without the infrared readings from the panel below and provides an acceptable estimate.

A summary of average heat losses and total panel efficiencies is provided in Table 16, along with heat loss values predicted from a panel radiation and convection model. From these data and analysis it is clear that the quartz tubes have a significant effect on panel efficiency, and implies that convection blocking mechanism should be incorporated into the final design. It also shows how the model can be improved. Error in the vertical cases can be attributed to wind, and in the windowless horizontal case to convection that was not accounted for. These can be accounted for with a wind speed and direction correction factor.

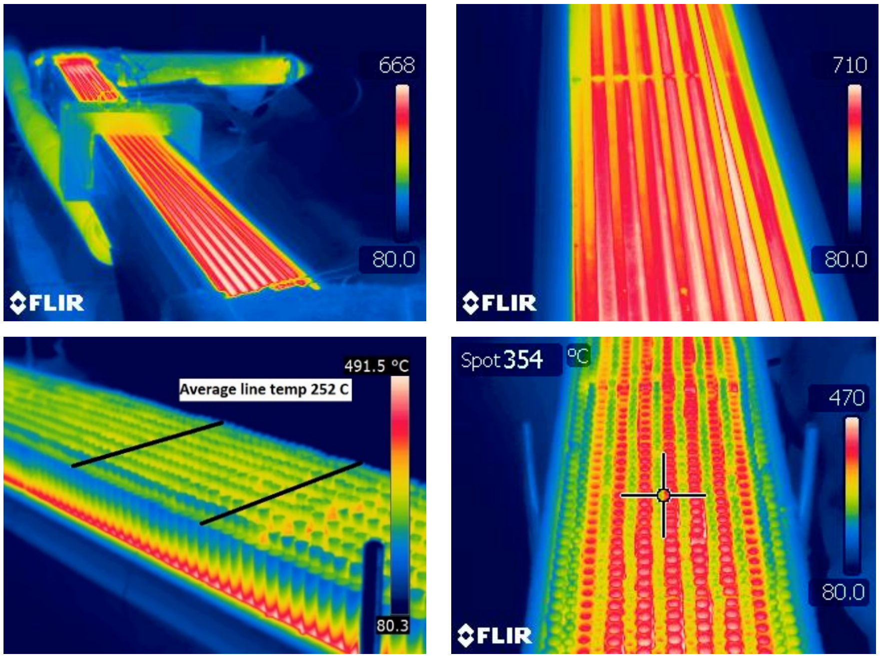

Figure 49 – A comparison of temperature profiles in horizontal tests without (top), and with (bottom) quartz tubes.

Table 16 – Predicted and measured heat loss, and uncorrected calculated efficiency (from measured data) for the 9 test cases.

	Predicted Heat Loss (kW)	Avg. Heat Loss (kW)	Efficiency
Case 1	37.07	43.18	92.62%
Case 2	46.5	61.09	89.55%
Case 3	48.65	52.84	90.96%
Case 4	50.93	51.63	91.17%
Case 5	27.27	32.25	94.49%
Case 6	23.13	24.97	95.73%
Case 7	21.57	22.83	96.10%
Case 8	26.22	25.09	95.71%
Case 9	26.24	26.06	95.54%

Data Reduction and Corrected Results

The primary challenge in reducing the acquired data is in establishing representative back-to-back comparisons. Due to changing ambient conditions (wind speed, temperature) and test conditions (cell surface temperatures), corrections were applied to estimate the true benefit of the quartz window. The following details describe this correction process and reference the values shown in Table 17.

The test case that produced a cell surface temperature closest to that of the anticipated application – i.e, the 90° incident wind direction case with window – was selected as the baseline case. Therefore all other cases were corrected to “match” the test conditions of the baseline case.

Variations in ambient and cell surface temperature will result in different levels of convection and radiation losses from the cell. To account for this:

- The average cell surface temperature T_{surf} is calculated for each test

- Since convection losses are proportional to (T_{surf}-T_{amb}), that value is calculated for each test. The value of that difference is normalized to the value in the baseline case, thereby generating a scaling factor for the convection that might be expected if the surface and ambient temperatures matched those of the baseline case.
- Likewise, since radiation losses are proportional to (T_{surf}^4-T_{amb}^4) that difference is calculated for each test. The value of the difference is normalized to the value in the baseline case, thereby generating a scaling factor for the radiation that might be expected if the surface and ambient temperatures matched those of the baseline case.
- HOWEVER, the exact ratio of convection losses-to-radiation losses is not known for any of the cases; the test treats the losses as a combined loss. That said, the situation may be bracketed by assuming a range of convection/radiation loss ratios. Therefore three bracketing ratios were evaluated for each case:
  - Losses = 20% convection, 80% radiation
  - Losses = 50% convection, 50% radiation
  - Losses = 80% convection, 20% radiation

Table 17 – Raw data, correction factor calculations, and corrected data for 5 vertical-orientation test cases

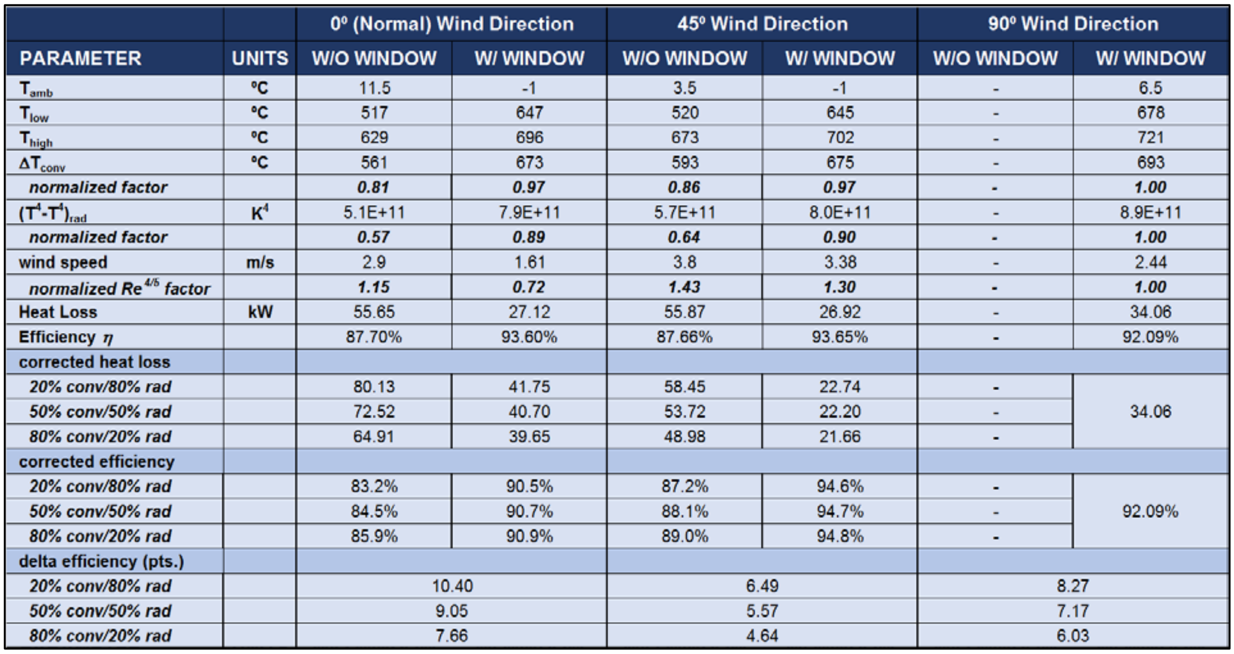

		0º (Normal) Wind Direction		45º Wind Direction		90º Wind Direction	
PARAMETER	**UNITS**	**W/O WINDOW**	**W/ WINDOW**	**W/O WINDOW**	**W/ WINDOW**	**W/O WINDOW**	**W/ WINDOW**
T_{amb}	ºC	11.5	-1	3.5	-1	-	6.5
T_{low}	ºC	517	647	520	645	-	678
T_{high}	ºC	629	696	673	702	-	721
ΔT_{conv}	ºC	561	673	593	675	-	693
normalized factor		***0.81***	***0.97***	***0.86***	***0.97***	-	***1.00***
$(T^4\text{-}T^4)_{rad}$	K^4	5.1E+11	7.9E+11	5.7E+11	8.0E+11	-	8.9E+11
normalized factor		***0.57***	***0.89***	***0.64***	***0.90***	-	***1.00***
wind speed	m/s	2.9	1.61	3.8	3.38	-	2.44
normalized $Re^{4/5}$ factor		***1.15***	***0.72***	***1.43***	***1.30***	-	***1.00***
Heat Loss	kW	55.65	27.12	55.87	26.92	-	34.06
Efficiency η		87.70%	93.60%	87.66%	93.65%	-	92.09%
corrected heat loss							
20% conv/80% rad		80.13	41.75	58.45	22.74	-	34.06
50% conv/50% rad		72.52	40.70	53.72	22.20	-	
80% conv/20% rad		64.91	39.65	48.98	21.66	-	
corrected efficiency							
20% conv/80% rad		83.2%	90.5%	87.2%	94.6%	-	92.09%
50% conv/50% rad		84.5%	90.7%	88.1%	94.7%	-	
80% conv/20% rad		85.9%	90.9%	89.0%	94.8%	-	
delta efficiency (pts.)							
20% conv/80% rad		10.40		6.49		8.27	
50% conv/50% rad		9.05		5.57		7.17	
80% conv/20% rad		7.66		4.64		6.03	

Wind speed was another variable that was not constant through all of the testing. Again, the precise behavior of wind along the surfaces of the cells was unknown, but bracketing assumptions were again applied. At one extreme the heat transfer loss due to wind speed was assumed to be proportional to $Re^{0.8}$, corresponding to the Nusselt number correlation for flow over a flat plate. On the other extreme, the heat transfer loss was assumed to be proportional to $Re^{0.1}$, suggesting that the heat loss mechanism is relatively insensitive to the wind speed, which would be the case if there was very little interaction between the far-field wind stream and the majority of the cell surface. Again, the ratio of the Reynolds Number correction factor for the non-baseline/baseline case was calculated, and used to correct heat losses from the non-baseline case to what might be expected under baseline wind speed conditions. Note that the latter case described above – in which there is limited interaction between the far-field wind velocity and the cell surfaces – may be accurate; the tightly spaced cells in close proximity to their neighbors, in contact on their tail end with a solid insulation board, essentially creates multiple dead-headed chambers which may not see much direct thermal communication with the wind, and instead be more significantly dominated by internal natural convection cells.

By applying these assumptions, the measured heat loss results for every non-baseline case was corrected to estimate the corresponding losses if the cell surface and ambient temperatures were those of the baseline case.

While further investigation of tube attachment techniques is necessary to make this design concept practical, the test has demonstrated the substantial benefit of a convection blocking quartz tube window. For all corrected windowed cases shown above, the receiver efficiency exceeds the 90% target. Note that this testing has also provided empirical data to refine heat loss models; Brayton is currently working with a group at the University of New Hampshire (UNH) to develop and accurate receiver heat loss model.

Cell Stress and Flux Tolerance Analyses

Brayton has continued its effort to model the absorber cell structure to further understanding of its thermal and structural performance in operation. Figure 50 and Figure 51 depict previously presented FEA results of these stress analyses; Figure 52 shows detail of the life-limiting feature, the stress concentration at the terminal fin fillet – i.e. the braze fillet at the last fin adjacent to the cell nose. Table 18 summarizes results of this study, showing the effect of various configuration and material variations.

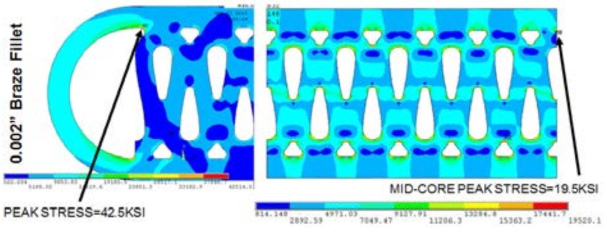

Figure 50 – FEA Stress results with 0.002" braze fillets.

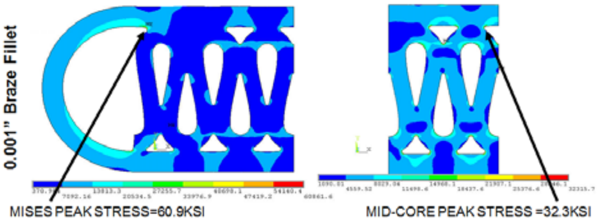

Figure 51 – FEA Stress results with 0.001" braze fillets.

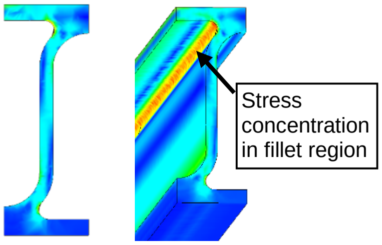

Figure 52 – Stress distribution for FEA model of folded fin with fillet

Table 18 – Comparison of stress levels for various design configurations

FLUX (kW/m^2)	STRESS (MPa)	STRESS (psi)	IN617 (hrs)	IN625 (hrs)	H214 (hrs)	H224 (hrs)	H230 (hrs)
48 FPI/ 0.006 Fin	63.54	9,215.13	96,131	16,696	13,140	674	17,302
57 FPI/ 0.004 Fin	87.02	12,621.08	7,503	1,334	3,682	111	1,963
60 FPI/ 0.008 Fin	27.84	4,038.09	77,355,420	12,641,476	369,759	77,055	5,219,582
# 30 Mesh	64.04	9,287.79	90,190	15,673	12,729	644	16,385
# 10 Mesh	174.52	25,311.49	27	5	221	2	16

A detailed analysis of flux capacity for the proposed receiver cell architecture has been investigated to provide insight regarding temperature distribution around the critical region (i.e. terminal fin fillet) of the cell exposed to flux.

Results of the study have been used to develop models to predict maximum metal temperatures as a function of incident flux and fluid temperature. An alternative closed-nose cell configuration has been evaluated to determine its viability as a means of eliminating the elevated stress concentration factor of the terminal fin and thereby extend the absorber cell life. An image of this configuration is shown in Figure 53. Probe locations for maximum nose and braze temperature (T_n, T_b) are shown, as well as naming convention for flow channels.

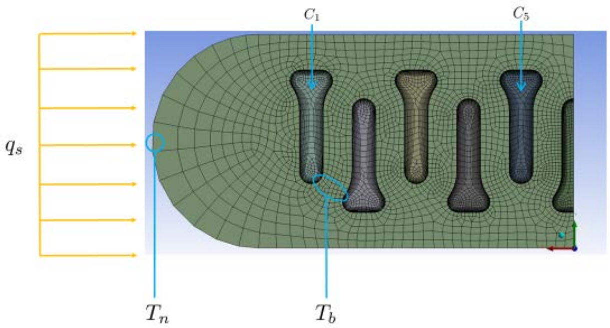

Figure 53 – CFD model for flux validation study showing flux vector (yellow) and temperature gradient from the nose (T_n) to the braze (T_b)

A parametric study of temperature distribution for different cell geometry subject to varying flux values was investigated.

Values for the study are included in Table 19. Mass flow per channel (C1, C2, etc.) are prescribed such that the ≤5% receiver pressure drop limit is always satisfied.

Table 19 – Range values for CFD parametric study.

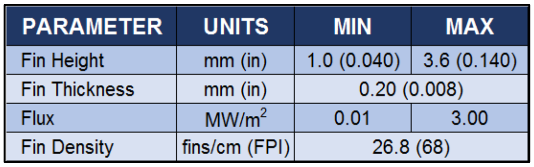

PARAMETER	UNITS	MIN	MAX
Fin Height	mm (in)	1.0 (0.040)	3.6 (0.140)
Fin Thickness	mm (in)	0.20 (0.008)	
Flux	MW/m^2	0.01	3.00
Fin Density	fins/cm (FPI)	26.8 (68)	

Results from this study were used to develop predictive models for maximum nose (T_n) and braze (T_b) temperatures as functions of bulk channel fluid temperature and normal flux. An example of a typical temperature profile across cell nose is shown in Figure 54.

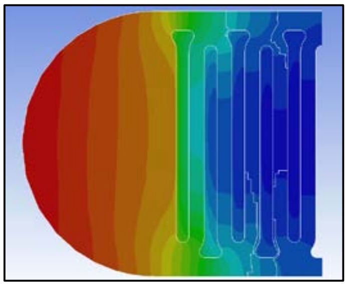

Figure 54 – Example temperature distribution at nose section of filled –nose receiver cell.

Final results representing the current receiver were generated by constraining the maximum nose metal temperature to 790°C at any point along the receiver. The resulting values for maximum flux and predicted braze temperatures are presented in Table 20. Note that the decreased braze temperatures predicted corresponds to significant improvement in Creep & Fatigue performance capacity for this absorber cell architecture.

Table 20 – Results from CFD flux validation study.

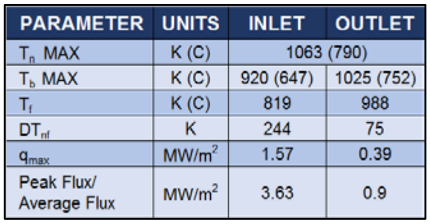

PARAMETER	UNITS	INLET	OUTLET
T_n MAX	K (C)	1063 (790)	
T_b MAX	K (C)	920 (647)	1025 (752)
T_f	K (C)	819	988
DT_{nf}	K	244	75
q_{max}	MW/m^2	1.57	0.39
Peak Flux/ Average Flux	MW/m^2	3.63	0.9

Final Receiver Cell and Panel Geometries

Predictive models developed from fatigue and creep tests are used to define design parameters required to achieve the lifing goals listed in Table 21. Combining the creep model with the equivalent stress formulations yields a

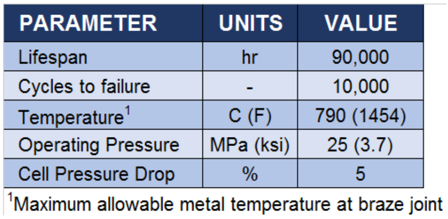

PARAMETER	UNITS	VALUE
Lifespan	hr	90,000
Cycles to failure	-	10,000
Temperature[1]	C (F)	790 (1454)
Operating Pressure	MPa (ksi)	25 (3.7)
Cell Pressure Drop	%	5

[1] Maximum allowable metal temperature at braze joint

Table 21 – General life parameters for receiver cell architecture.

concise expression which describes the upper design limit for the average section stress,

$$\bar{\sigma} < \sigma_r \tag{9}$$

Developing (9) for the inboard fin using (4) and (6) yields the following relation,

$$\delta \cdot f_{pi} > \left[\left(\frac{\sigma_r}{\bar{k}_t \cdot p_i}\right) - 1\right]^{-1} \tag{10}$$

The resulting graphs of minimum fin density versus rupture time for various configurations for both Inboard and Terminal fins are presented below in Figure 55 and Figure 56. These predicted results correspond to IN625 structures at the pressure and temperature conditions in Table 22.

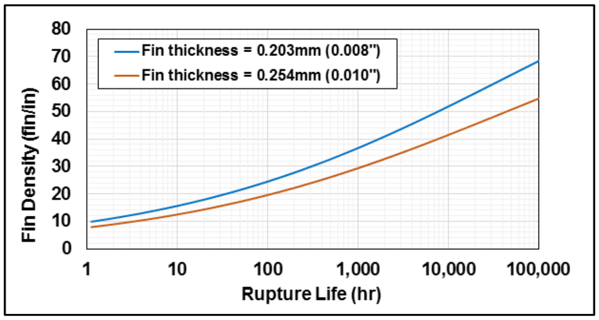

Figure 55 – Minimum fin density versus creep rupture time for Internal Fin.

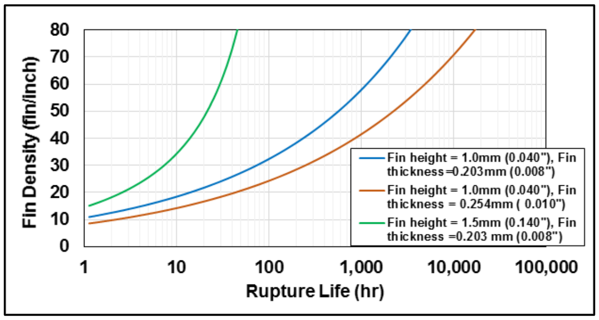

Figure 56 – Minimum fin density versus creep rupture time for Terminal Fin.

Current manufacturing methods limit the maximum achievable fin density to 80fin/inch (fpi). thickness up to 0.254 mm (0.010”). Given this fin density constraint the predicted time to rupture for the unsupported Terminal Fin configuration is less than 18,000 hours (refer to Figure 56). Referring to Figure 55, results for the Internal Fin show that the minimum requisite fin density to reach the design lifespan (90,000h) is achieved well within margin (80fpi) as listed in Table 22.

Table 22 – Minimum fin density for Internal Fin attendant with lifing criteria in Table 21.

FIN THICKNESS mm (in)	FIN DENSITY fins/cm (fpi)
0.203 (0.008)	26.4 (67)
0.254 (0.010)	19.7 (50)

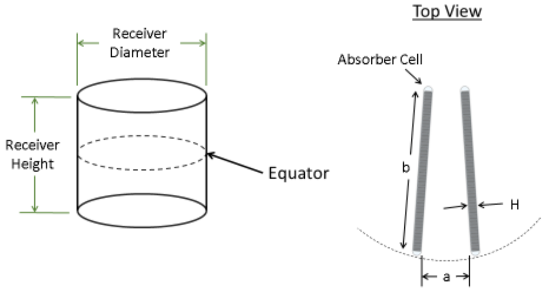

Figure 57 – General design parameters optimized using receiver model.

Table 23 – Primary constraints applied during receiver geometry sizing.

PARAMETER	UNITS	MIN	MAX
Receiver Diameter	m	2	5
Geometric Concentration Ratio	-	600	-
Cell Pressure Drop	%	-	5
(Peak Flux/Average Flux) per cell	-	1.5	-

In order to attain the necessary fin density a post-compaction process is performed to the folded fin. This process has been developed and refined for fin thicknesses through 0.203 mm (0.008).

Note that minimum fin density, thickness parameters required to achieve fatigue lifing requirements as outlined in Table 22 are satisfied with generous safety margin.

Final dimensions of the absorber cell are generated using detailed models describing entire external receiver design. Through iterative refinement the dimensions of the absorber cell. Once minimum absorber design structural requirements have been established, the Receiver Diameter/Height is determined (refer to Figure 57) through optimization within the constraints shown in Table 23. Final results for the dimensions of the absorber cell and receiver are presented below in Table 24. In addition to meeting life requirements, the resulting receiver configuration produces a number of corollary results that are critical to the performance of the overall CSP system. Specifically:

- Geometric Concentration Ratio =
  $A_{field(w/o\ field\ multiplier)}/A_{aperture} = 648$
- Flux at Receiver Equator = 1.49 MW/m^2
    - Flux margin at Equator = 5.4%
    - By comparison, typical steam boilers operate at 60-250 kW/m^2[vi]
- Allowable Outlet Flux = 390 kW/m^2
- Average Receiver Flux = 413 kW/m^2
    - PeakFlux/AverageFlux = 3.6
- T_{nose} = 790 °C along cell length
- $T_{braze} \leq 752$ °C along entire length
    - N.B.: 90,000 hour creep life limit is T_{braze} = 790 °C

This analysis indicates flux margin at all points on the absorber surface; the implication being that the absorber is tolerant to flux anomalies.

Table 24 – Dimensions of absorber cell and receiver geometry.

PARAMETER	UNITS	VALUE
CELL GEOMETRY		
Material	-	IN625
Fin Density	fin/in	68
	fins/cm	26.8
Fin Height	in	0.09
	mm	2.29
Fin Thickness	in	0.008
	mm	0.2
Boundary Thickness (t_f)	in	0.01
	mm	0.25
Cell Total Height (H_f)	in	0.11
	mm	2.62
Cell Length (L_f)	in	79.76
	m	2.03
Cell Flow Width (W_f)	in	3
	mm	76.2
RECEIVER GEOMETRY		
Receiver aperture area	m^2	51.54
Cylindrical Diameter (D=H)	m	4.05
Concentration Ratio		649
Total Number of Cells	-	1165
Cell spacing aspect ratio	-	4
Cell spacing	m	0.019
	in	0.75
Cell gap	mm	16.256
	in	0.64

Annualized Receiver Performance

With the finalized dimensions selected in order to meet the design point performance (which in itself is a function of material surface temperature, radiation view factors, quartz window benefits, etc.) and receiver duration/life (i.e. creep life, fatigue life, etc.), the methodology developed in prior program phases was applied to determine the annualized efficiency.

Table 25 – Tabular summary of the Receiver Annualized Efficiency for both windowed and non-windowed cases.

PARAMETER	*UNITS*	WINDOW BASELINE	NON-WINDOW TEST CASE
Analysis Case	-	Barstow CA, 2009 Weather Data	
Efficiency (850 DNI)	-	90.62%	78.36%
Annualized Efficiency	-	88.36%	72.99%
Total annual losses	kW_{th}	8,940,000	20,800,000
Thermal power in (850 DNI)	kW_{th}	22,222	
Total annual energy in	MWh	76,900	
Receiver collection area	m^2	51.53	
Receiver D = L	m	4.05	

Solar and meteorological data for Barstow, CA was selected as a representative installation location, and the annualized efficiency was calculated on that basis (Table 25). Governing operational assumptions (operational threshold insolation level, power generation profile, etc.) were applied, along with validated absorber surface temperature models, convection and radiation loss models based on experimental test results, and appropriate reflection and system integration assumptions. The resulting calculated annualized efficiency for this receiver, at 88.4% for the windowed case, represents a performance that exceeds the state-of-the-art tubular boiler receiver operating at much lower steam temperature.

It should be noted that dimensions shown in Table 24 do not represent optimized values; rather, they are a configuration that meets the receiver performance and life requirements given the assumptions and systemic simplifications (sCO_2 cycle performance, heliostat performance, etc.) applied in the analysis. More importantly, this program has resulted in a methodology and suite of tools that can be used to identify true optimums for a specific well-defined application.

Manifold Design

Having identified the layout of the receiver, an area of critical importance to the design of the system is the manifold. The original concept – consisting of thick-walled pipes into which cells are welded and/or brazed – was determined to be functional and achievable, but also expensive and heavy. Further development, reported at length previously, resulted in a cell-based cap-and-sleeve manifold design that was inexpensive, modular, and lightweight.

The new modular header design consists of two pieces at each end of the cell, all shown in Figure 58. The first, shown on the left, is the distribution gallery. It consists of a small block of machined or cast metal that has a width matching that of the cell to be headered. Flow enters (or leaves) the gallery from the end (or the back face), and distributes through multiple hole features along its side.

The second piece – shown in the center in Figure 58 – consists of another block, into which is machined or cast a cut to receive the candidate absorber cell. Because this cell-attachment block is small, it may be brazed as part of the cell assembly braze step (or, if preferable, as a secondary braze operation). Note that, as described above, brazing the cell into this receiving piece fills the fit-up gap with braze material, providing the support necessary to react the internal pressures at the ends of the cell, and thereby eliminating any chance of end failure.

The first and second blocks just described mate to each other along their long faces; to accommodate this they each have an appropriate weld prep area machined or cast into them. Once a second block has been brazed to the cell at either end, they are welded to the first blocks to form a cohesive sub-header, as on the right in Figure 58.

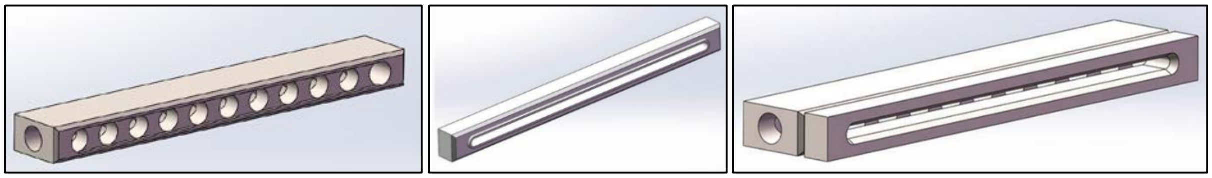

Figure 58 – Header cap (left), header sleeve (middle), and header weldment (right).

One full header and cell assembly is depicted in Figure 59. Note that there is a corresponding assembly at the opposite end of the cell.

Because these block pairs are modular they are sized to the cell, not the full heat exchanger core; as a result they never require the exceedingly heavy thick wall dimensions required by larger flow areas to support the high internal pressure.

Multiple cells are then stacked together to form a full core, as shown in Figure 60. Adjacent header blocks are welded to each other. This results in the advantageous strain-compliant core design Brayton has described in previous reports. The welded headers are structural and rigid, but the cells themselves are allowed to move and flex to relieve thermal-induced strains.

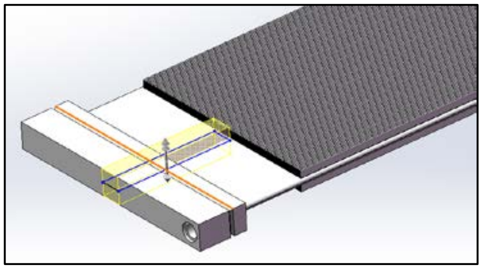

Figure 59 – Fully headered cell assembly; the cell is brazed into the sleeve block, which is then welded to the endcap. This procedure is performed at each end of the cell.

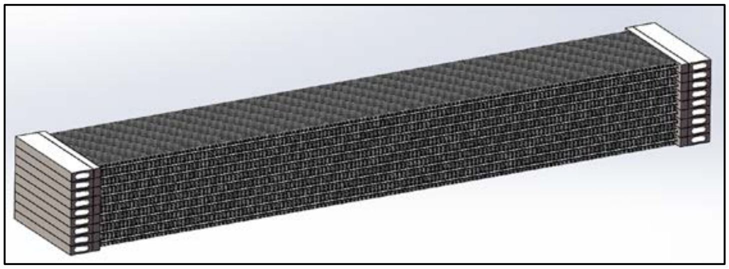

Figure 60 – A full core assembly, with multiple headered cells welded to each other. Each cell is capable of moving out-of-plane from its neighbors to alleviate thermal strain. The fluidic connections are into the ends of the header blocks.

Once the full core stack has been assembled and welded, a semicircular manifold is welded along the manifold block face and over the inlet/outlet ports (Figure 61). Because this manifold is independent of the cell dimensions, it may be sized for the core flow pressure drop requirements, and need not be any larger. This minimizes the wall thickness needed, reducing weight and cost. It also results in a very compact manifold.

Figure 61 – Schematic image showing the semicircular flow gallery to be welded onto the manifold block. Flow in the semicircular channel will distribute into or collect from the flow ports on each of the manifolded endcaps

Brayton performed rigorous stress analyses on the structure to ensure that it could see service in the high pressure sCO_2 applications for which it was intended. An FEA model and some corresponding stress results are shown in Figure 62. The determination was that these modular headers are appropriate for the intended applications.

Figure 62 – FEA model of the fully assembled cell, header sleeve block, and header end-cap block. The model mesh is shown on the left, and stress contours are shown in cutaway on the right.

Figure 63 shows a single cell that was assembled using this header design for a sCO_2 pre-cooler. In contrast to the SunShot receiver design, the outer surfaces of each cell has a cross-flow fin. Otherwise, the general architecture is directly comparable. Figure 64 and Figure 65 both show the manifold assembly for the entire core with a semicircular gallery welded to the end face and a single fluidic connection to the core. Again, ignoring the external fins, this construction is precisely analogous to the absorber panel module developed by Brayton for this program.

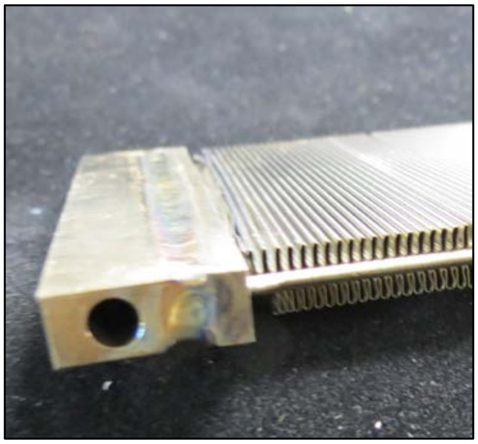

Figure 63 – Full cell and manifold assembly, showing the welded 2-piece manifold assembly (left) with its mated brazed cell (right).

Figure 64 – Full heat exchanger core assembly, showing multiple manifolded cells welded together and capped with a semicircular flow channel. A single fluidic connection is welded to the semicircular flow channel.

Figure 65 – Assembled core consisting of multiple cell subassemblies welded together at the manifolds and capped with a flow channel and connection.

Finally, Figure 66 shows a completed heat exchanger core, including manifolds. Note the dramatic reduction in manifold size compared to previous designs. In form this is comparable to a solar absorber panel assembly, with multiple cells mounted in parallel with a common header at each end, to be oriented vertically with the cell noses facing the incoming insolation.

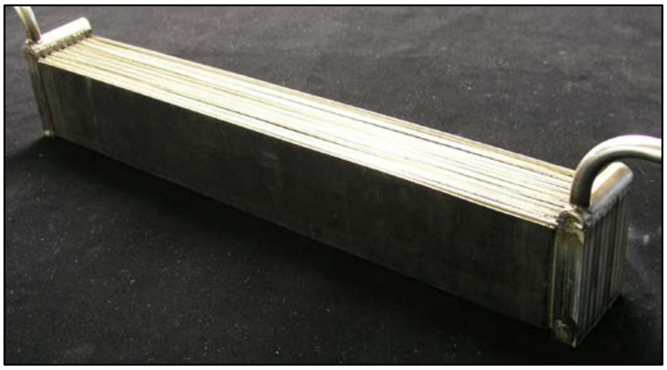

Figure 66 – View of a fully assembled heat exchanger core manifolded as described in this section. Nota that this assembly – minus its external fin sets and with narrower cells – is analogous to a single absorber panel module as defined in this program.

Commercial Receiver Layout

The Brayton solar absorber is designed to be manufactured, a factor key to reducing the system cost by eliminating on-site engineering and construction. Individual absorber cells (Figure 12) are brazed, headered and manifolded, (Figure 66), and then assembled into panels (Figure 67, Figure 68) incorporating Brayton's quartz tube window.

Brayton has defined a suitable layout that not only provides structural support for the system, but also accommodates the thermal growth experienced by the cells during high-temperature operation. In contrast to the monolithic header structure depicted in

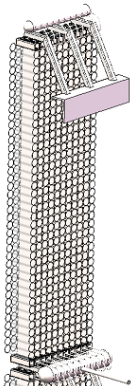

Figure 67 – Panel module with quartz tube window.

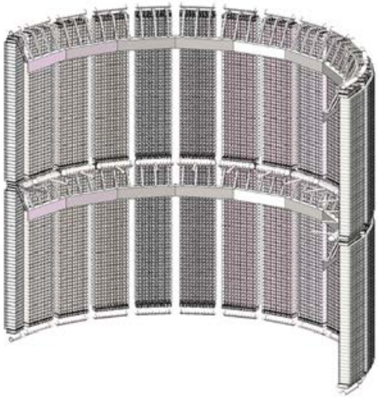

Figure 68 – Cutaway view of full receiver assembly with multiple panels around aperture.

Figure 66, cells are mounted separately by securing their individual header blocks in metallic spring clips (Figure 69). This configuration allows for thermal strain relief in both the vertical and horizontal directions – as shown in Figure 70 – and supports the cells by allowing them to hang. Individual fluidic connections are made to each header block behind the insulation board (Figure 71); the connections are thin curved to provide flexibility and strain relief. These are in turn connected to the main panel manifold at either end of the cells.

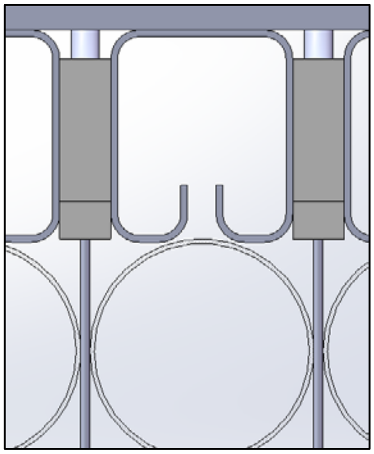

Figure 69 – Close-up of absorber cells (vertical) and header blocks captured by spring clips, with quartz tubes mounted between cells.

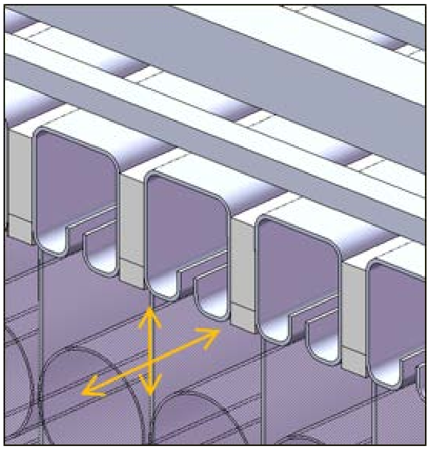

Figure 70 – Close-up of absorber cells and header blocks captured by spring clips, showing degrees of freedom to relieve thermal strain.

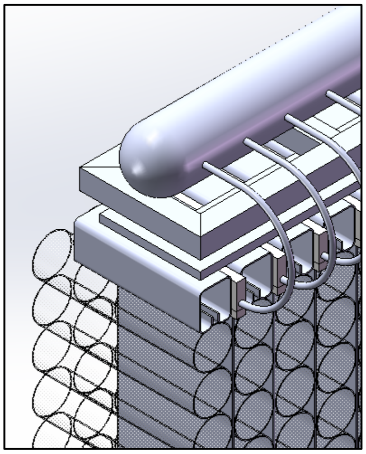

Figure 71 – Image of the modular panel assembly, with backside fluidic connections between header blocks and manifolds.

Figure 72 – Two-panel module with shared central inlet manifold.

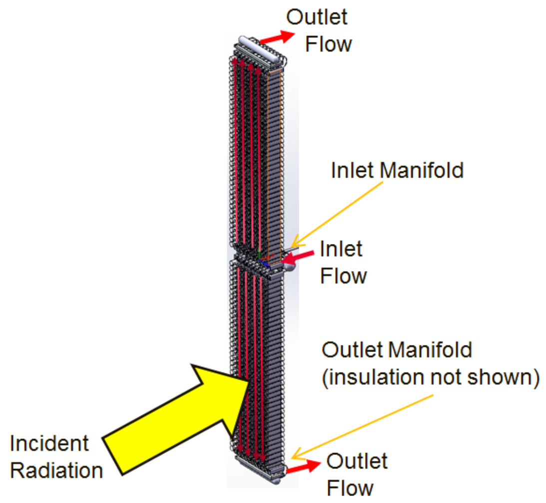

Figure 73 – Schematic showing flowpaths within the two-panel receiver module; receiver inlet flow enters through the central manifold, distributes up and down through absorber cells, and then collects at manifolds at either end.

Pairs of panels are further assembled into receiver modules (Figure 44, Figure 72); and are plumbed into the system such that the fluid inlet is at the central manifold, distributing in parallel through cells above and below (see Figure 73).

Full receiver modules, once factory-assembled and shipped via truck to the installation site, are installed upon the central tower. Each module is situated along the circumference of the receiver, producing a cylindrical aperture surface (Figure 74, Figure 75). This form factor has been well-vetted, and is seen in state-of-the-art solar receiver towers such as the Solar Reserve installation seen in Figure 76.

Neighboring panels are mounted in close contact, such that there is no gap between adjacent modules. The highest flux levels, which are located along the equator of the cylinder due to the optical characteristics of the heliostat field, are absorbed through a header block design which uses the low inlet-temperature full cell flow to manage the local material temperature.

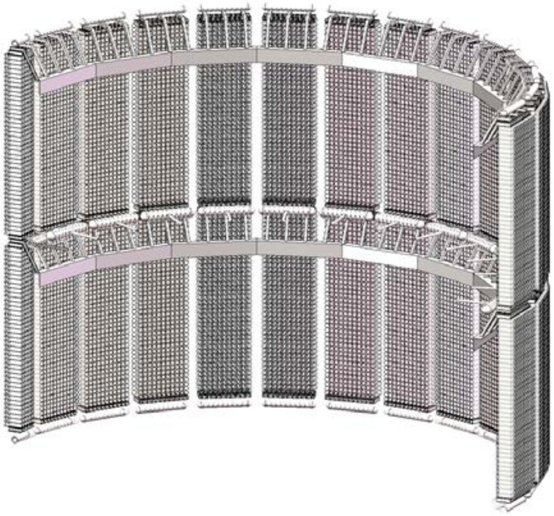

Figure 74 – Cutaway view of receiver, showing multiple modules mounted around aperture circumference.

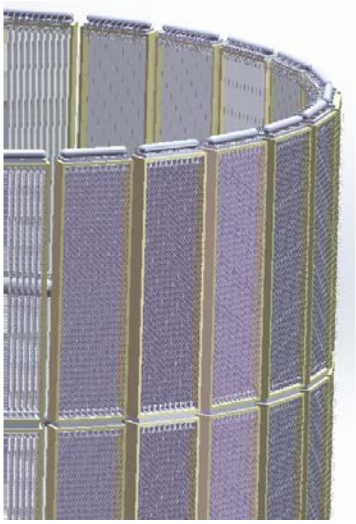

Figure 75 – External view of receiver with multiple modules.

Figure 76 – Solar Reserve cylindrical receiver.

Manufacturing Plan

Critical to the success of this program is the development of a low-cost manufacturing plan that is capable of producing the required absorber cells and receiver components robustly, reliably, and repeatably.

Table 26 – Manufacturing process outline and description

STEP	PROCESS	TYPE	DESCRIPTION
1	**Internal Fin Processing**	Toll Processing, Direct Labor	Receive folded fin, cut fin, compact fin
2	**Panel**	Toll Processing	Receive formed plates
3	**Header**	Direct labor	Extruded rod, progressive machined
4	**Part Cleaning**	Direct Labor	Load part washer, wash parts, unload parts, inventory
5	**Braze Alloy Application**	Direct Labor	Load spray booth, begin sequence, remove panels, inventory
6	**Cell Assembly**	Direct labor	Assemble cell parts and CD weld in panel weld fixture
7	**Cell Panel Weld**	Direct Labor	Convey fixture cell to weld station, weld sequence
8	**Fixture for Brazing**	Direct labor	Assemble cells into graphite braze fixtures
9	**Furnace Braze**	Direct labor	Load furnace, braze, unload, defixture and visually inspect cells
10	**Header Assembly**	Direct labor	Fixture header, apply braze paste, visually inspect
11	**Header Re-Braze**	Direct labor	Fixture cells, load furnace, furnace cycle, unload furnace, unfixture, visually inspect
12	**Cell Pressure Test**	Direct labor	Fixture, run test, record results, unfixture

Brayton intends to leverage experience in developing manufacturing processes for high temperature and high pressure heat exchanger systems to generate this manufacturing development plan for the solar absorber panels. The absorber panels share many of the components that are involved in the familiar processing of fluid-fluid heat exchangers, and are in fact a simpler construction. The manufacturing process for these panels has been outlined and is summarized in Table 26.

This process is based on a standard practice for the current best understanding of the design. The process is subject to change considering the detailed product design, however it is not expected to deviate substantially. Note that at the time of this writing, the process description provided summarizes only the manufacture of the absorber panels and header system to interface with working fluid supply piping. System integration and installation will be discussed at a later time with a more complete understanding of the system layout.

Table 27 – Assumed production rates

Cells per Unit (approx.)	1,200
Units per year	10
Total Cells	12,000
System Power (MW_e)	10
Power Manufactured (MW_e/yr)	100

This process assumes that the factory be sized to deliver a product volume capable of 200MWth per year. This equates to an estimated 12,000 absorber cells per year. Rates are summarize in Table 27 below.

The process outlined in Table 26 is discussed in detail in the following section. A more detailed description of the process is presented with estimates on the type and quantity of equipment needed and the impact on the direct labor necessary.

Process Step 1 – Internal Fin Processing

The process outlined assumes that the folded fin would be supplied by a fin folder. The price of this is well understood from Brayton's history with manufacturing heat exchangers. The fin is received and inspected. The fin is then subject to a compaction process to increase the fin density beyond that which is possible from the supplier. Brayton is familiar with the process on a small scale production level, however additional development is necessary to scale production rates to meet the demands of 1000 cells/month. An image of a prototypical fin compaction rig and resulting fin is shown in Figure 77.

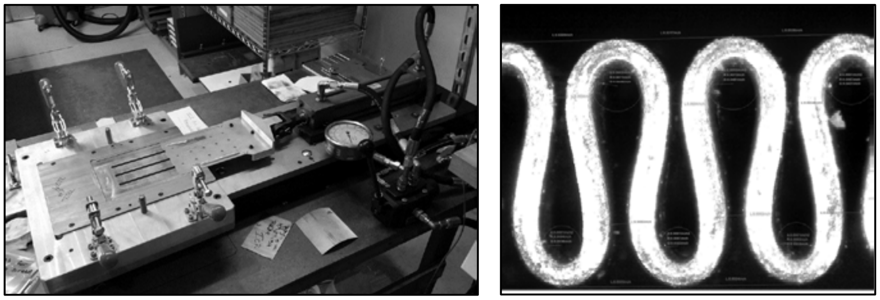

Figure 77 – Prototype fin compaction rig (left) and compacted fin product (right).

Process Step 2 – Panel

Brayton intends to utilize a die forming supplier to form the panels. The supplier will likely use a progressive die-form operation to achieve higher throughputs and lower part costs. Supplier quotes for similar part geometry and production quantities. Figure 78 shows the panel profile that will be used in the absorber panel design.

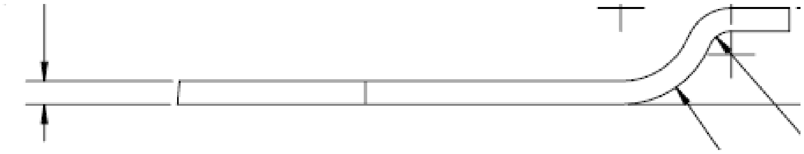

Figure 78 – Typical panel profile is a 2 dimensional bend and lends well to high throughput form or brake operations

Process Step 3 – Header

Brayton will employ a single piece header design replacing the two piece header sleeve and cap design concept that has been discussed in previous discussion. This design change eliminates the need to weld the cell to the sleeve and the cap to the sleeve, reducing the manufacturing costs associated with preparing header details and header-cell integration.

Extrusion techniques would utilize a near-net shape rectangular bars that would be cut to length. A multistep machining operation would be used with multi-part "tombstone" fixtures for detail machining. The nature of the design allows for machining from a single plane, eliminating the need for costly re-orientation and re-fixturing.

Figure 79 – Prototype header machined from IN625 plate stock.

Process Step 4 – Part Cleaning

Part cleaning will be accomplished with a batch part cleaner. Brayton is familiar with this type of process and utilizes similar equipment for our current operations. Pricing is based on previous supplier quotes that have been obtained for similar programs. Due to the increased size of the solar absorber panels, a premium was placed on the quotes for a marginally larger machine. Experience with this type of process dictates the process times and subsequently the number of stations necessary to meet demands.

Process Step 5 – Braze Alloy Application

Brayton applies powder braze alloy to cell panels with a proprietary adhesive. The adhesive spray and powder alloy application is a familiar process to Brayton at small scale production levels (~100 parts/month) utilizing a hand spray gun and manual powder application. Meeting 1000 parts/month will require an automated spray and powder application system. This process is familiar to Brayton, as applied to the recuperator manufacturing experience. While masking is necessary at low volume production, it is not needed when using an automated spray arm. Estimates for system pricing is based on Brayton's previous experience with high volume recuperator production and through consultation with robotic vendors.

Process Step 6 – Cell Assembly

Cell assembly consists of integrating the fin and panels prior to welding the 2 panels together. The parts are assumed to be cleaned and free of grease or oils. Operators handling the parts are expected to wear rubber gloves to avoid oils from fingers and hands to be transferred to the parts that will subsequently be brazed. The panel will have previously been coated with the correct amount of alloy.

It is assumed that an operator will manually assemble the cells aided by ergonomic assembly fixtures. The operator will place the bottom panel, place the fin in the bottom panel, and place the top panel. A light capacitance discharge weld will support the cell during handling between assembly and welding. The assembly fixture will constrain the cell during assembly and panel welding. Pricing for assembly tables and fixtures is familiar to Brayton and is drawn from experience in developing such fixtures for low volume production.

Process Step 7 – Cell Panel Weld

Once assembled and properly constrained in a fixture or by resistance weld, an operator will fixture the cell into a linear actuated, dual torch PAW system. The system settings (speed and heat sequence) are assumed to be fully defined. The operator will activate the system which will weld the panel on both sides simultaneously. The current weld speed is approximately 8-12 in/min. During the weld process, the operator is free to conduct other tasks such as visual weld inspection, fixturing subsequent cells, stacking and inventory, or any other necessary ancillary operations. The pricing of the equipment is well understood by Brayton and only incremental improvements would be necessary to the current system to meet production demands for the solar absorber. Figure 80 shows the linear welding system and the resulting welded panel.

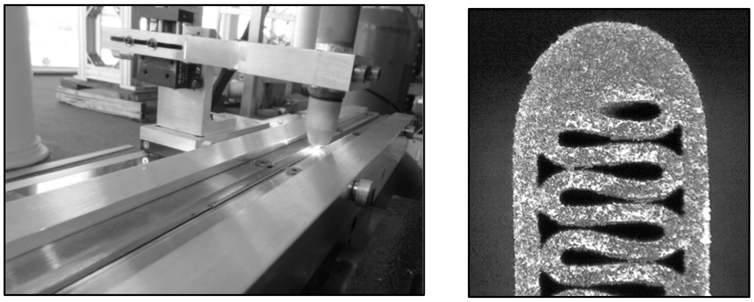

Figure 80 – Linear PAW panel weld system. Single torch system shown (left), section view of welded panel (right).

Process Step 8 & 9 – Braze fixturing and furnace brazing

The welded cells (which are now stable from the weld) are stacked into graphite braze fixtures. The braze fixtures will be coated with an oxide ceramic layer to prevent eutectic reactions with the cell panels. A thin ceramic fiber blanket will be laid between adjacent cells in the stack to avoid a diffusion bond between cells. Historically, as many as 20 cells have been stacked in a single fixture. However, due to the length of these cells, furnace cycle development would need to be conducted to dictate the optimal number of cells per fixture. A more modest number of ten cells per fixture has been chosen for this analysis. A proprietary spring system provides the pressures necessary for successful brazing. Once the cells have been assembled into the braze fixture, they are loaded into the furnace. A conservative estimate of five fixtures are assumed to fit into the batch, yielding 50 cells per batch. Again this will be optimized upon detailed analysis of the furnace cycle, however it is likely that higher yields are possible. Upon completion the cells are unloaded from the furnace and removed from the fixtures. Visual inspection is conducted on both cells and fixtures to assure no obvious damage has been incurred by either. If satisfactory, both cells and fixtures are inventoried to their respective location.

Costs for fixtures has been estimated, however the amount of fixtures on hand will be dictated by the number of cells able to be fit in the fixture. A conservative estimate is provided which includes extra fixtures for inventory and for waiting in furnace queue.

The braze furnace is assumed to be a large electric resistance element vacuum furnace. The furnace chosen is primarily dictated by the length of the cells. The brazing process is the most costly element of the manufacturing operation. Brayton is relying on capital cost estimates from previous supplier quotes for similar furnaces sized adequately to fit the cells.

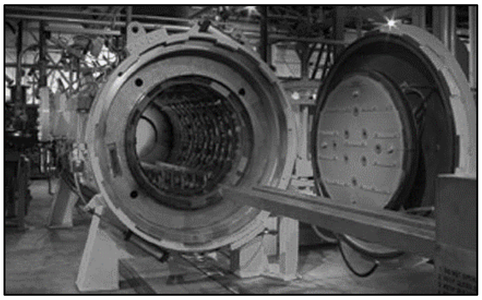

Figure 81 – Example vacuum braze furnace

Process Step 10 – Header assembly

Upon completion of the brazing cycle, cells are fitted with the header sleeve as illustrated in Figure 83. Note that the figure shows a heat exchanger cell for illustrative purposes, the procedure is identical for absorber panels. The operator will fit the header over the cell and apply paste to the backside of the header for a lower temperature braze sequence. At the proposed production rates, a separate furnace will be used for the re-braze cycle.

Figure 82 – Header sleeve being fit on a cell (left), braze alloy detail applied to back of header sleeve (right).

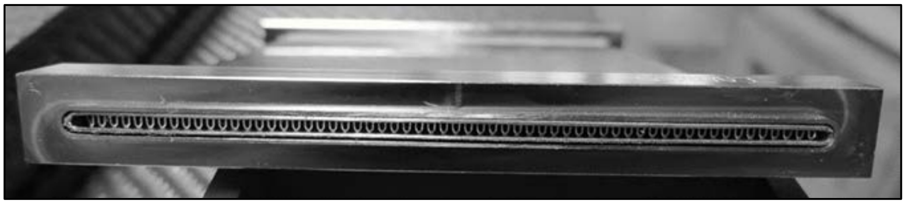

Figure 83 – Header sleeve being fit on a cell (left), braze alloy applied to back of header sleeve (right).

Process Step 11 – Header Re-braze

Due to the nature of the re-braze, significantly simpler fixturing is necessary and is reflected in the assumed costs. An operator will load and unload the furnace. Details of the fixtures are not defined, thus a similar furnace load is assumed until rigorous analysis on furnace cycle and loading is conducted. An illustrative example of cells prepared for re-braze is shown in Figure 84. The furnace used is assumed to be the same model number as with the initial brazing operation.

Figure 84 – Example of cells prepared for re-braze fixturing.

Process Step 12 – Cell pressure testing

The finished cell and header assembly is subject to a static pressure test at a pressure level that satisfies the design specifications. The pressurizing fluid is preferred to be incompressible (e.g.

water), however nitrogen or CO_2 are optional. An operator would manually load the completed cells into a purpose designed pressure test system, close seals, close a safety door, and activate a preloaded test sequence. Depending on the demands, the cell will be leak tested by monitoring pressure degradation over time, and also subject to elevated pressures to assure structural quality of the braze and weld joints. Upon completion of the test, the operator will remove the cell. If passed the cell will be inventoried for downstream processes. If failed, the cell will be subject to a failure analysis to determine the value of a repair. Common repairs are conducted on weld joints for leaks. In this case a cell will be manually repaired and subject to the pressure test. Braze joint failures are typically catastrophic and destroy the cell. This case results in reduced yield.

Semi-automated pressure test systems have not been developed by Brayton. Costs are based on an integration of manual fixtures and control systems that have been developed.

Subsequent processes

Additional processing is needed to integrate these cells into sub systems and ultimately the final product. Brayton is prepared to provide these estimates with further development of design details.

Manufacturing Examples

Since the inception of this program, Brayton Energy has successfully applied the technology being developed to commercial products. The following examples demonstrate the application of these new design and manufacturing processes to low-cost heat exchangers.

Gas Turbine Recuperators

Brayton Energy has substantial experience in vacuum furnace nickel brazing having delivered dozens of cores for gas turbine recuperators covering a wide range of design requirements. This equates to thousands of cells manufactured. See Figure 85 for an example of a fully-assembled recuperator core of this type.

Figure 85 – High temperature, low pressure gas turbine recuperator heat exchanger.

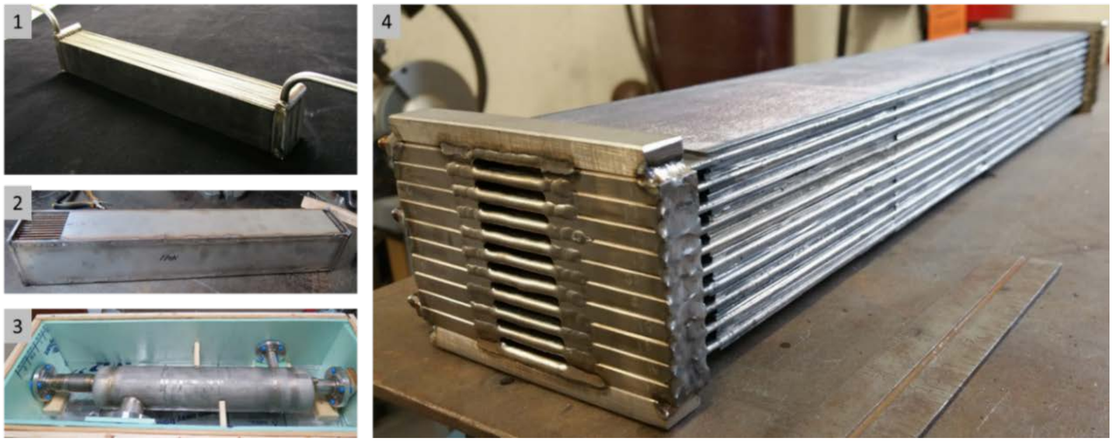

Figure 86 – High-temperature high-pressure heat exchanger core for use in a supercritical carbon dioxide cycle. (1) The headered core – consisting of multiple internal-fin-supported cells – with fluidic connections (2) The core mounted within the low pressure flow guide which directs a second flow countercurrent to the high pressure internal flow (3) The completed heat exchanger packaged within a pressure vessel, with flanged fluid connections (4) A close-up of the core, showing multiple cells connected together at their individual header blocks.

Supercritical CO_2 Systems

Brayton has delivered supercritical heat exchanger systems for several clients resulting in hundreds of successful brazed cells in several welded core assemblies. Figure 86 shows an example of this.

Receiver Cost

Brayton has continued its development of a highly detailed cost model for the receiver. The results of the cost model are shown in Table 28, which indicates a \$148/kW_{th} capital cost for the receiver and tower system with the inclusion of a 30% contingency.

Table 28 – Tabular breakdown of the Brayton Receiver costs, including tower and integration.

THERMAL POWER = 22,000 kW_{th}	RAW MATERIAL	LABOR AND PROCESSING	TOTAL	% TOTAL PANEL COSTS
PANEL SUBASSEMBLIES	**\$ 506,360**	**\$ 241,071**	**\$ 747,432**	**100%**
CELL	\$ 111,780	\$ 126,364	\$ 238,144	32%
FIN	*\$ 67,662*	*\$ 53,507*	*\$ 121,170*	*16%*
BALANCE OF CELL	*\$ 44,118*	*\$ 72,856*	*\$ 116,974*	*16%*
QUARTZ	\$ 186,402	\$ 49,333	\$ 235,735	32%
BALANCE OF PANEL	\$ 208,178	\$ 65,375	\$ 273,552	37%
	MANUFACTURING AND MATERIALS	**MOBILIZATION & INSTALLATION**	**TOTAL**	**% TOTAL TOWER COSTS**
TOWER AND SYSTEM PIPING	**\$ 844,882**	**\$ 900,000**	**\$ 1,744,882**	**100%**
TOWER	\$ 400,000	\$ 600,000	\$ 1,000,000	57%
DOWN PIPE (ENGINE SUPPLY)	\$ 393,280		\$ 393,280	23%
PANEL INSTALLATION		\$ 300,000	\$ 300,000	17%
BALANCE OF SYSTEM	\$ 51,602		\$ 51,602	3%
SYSTEM SUBTOTAL			**\$ 2,492,314**	
CAPITAL COST			**\$ 113**	**/kW_{th}**
30% CONTINGENCY			**\$ 747,694**	
SYSTEM TOTAL (W/ CONTINGENCY)			**\$ 3,250,000**	
CAPITAL COST			**\$ 148**	**/kW_{th}**

The cost model incorporates several key elements, which are integrated into a single cohesive system. These include:

- **Absorber Cells**: Brayton has extensive experience in the fabrication of heat exchanger cells for commercial clients, including the manufacture of the folded fin/shell architecture developed under the auspices of this program. This model is extremely rigorous and includes all aspects of the process, some internal details of which are:
  - *Cell Yield* is assumed to be 97% - i.e. 3% unplanned waste
  - *Fin Folding* is performed by Robinson Fin with semi-automated compaction
  - *Cell Shell* (parting plate) is an outsourced stamped part
  - *Batch furnace brazing*, using Metglas foil braze, with owned/operated furnace incurring \$50/hr costs incurred by operator (Brayton)
  - *Cell Header* is extruded and machined in tombstone fixture
- **Quartz Window**: Brayton has fabricated several quartz tube windows, and is therefore familiar with prototype window costs. Reasonable bulk order price reductions have been applied to generate production-level costs. The window cost assumes:
  - Equal number of nose and cell space pieces
  - Quartz welding – 15 seconds per tube silica cold weld

- **Modular Panel:** Brayton has extensive experience in packaging heat exchanger cores for fluidic control, thermal strain relief, containment, and structural support. This experience has been leveraged in the design and integration of the modular panel subassemblies.
    - Panel installation includes power piping installation (in addition to cranes, placement, and integration)
    - All fabricated structural steel assumed $4/lb (rolls up raw material and fab costs)
- **Integration and Tower:** Extensive investigation into the use of a commercial wind turbine tower for use with a CSP receiver has been performed as part of Brayton's APOLLO program. Discussions with both tower manufacturers and system integrators indicate that this is an attractive, viable, low-cost option for a receiver system of this scale. Conservative cost numbers from these sources are applied in the model.
    - Engine assumed at base of tower – includes 65m power process pipe 6" SCH160 IN625 ($400k)
- **Contingency:** A 30% has been applied to the cost model. Contingency covers lack of design definition on important, potentially costly aspects of program
    - Quartz tube containment
    - Insulation containment and structure
    - Shipping/Rigging
    - OSHA, Union, Tax, license, DOT, etc.

Note that conservatism has been applied wherever possible; therefore the engine is assumed to reside at the base of the tower (introducing a large piping cost), limited automation in the manufacture of absorber cells and panel components, etc. All details comprising this cost model are available for further review. A graphical breakdown of the system costs is shown in Figure 87.

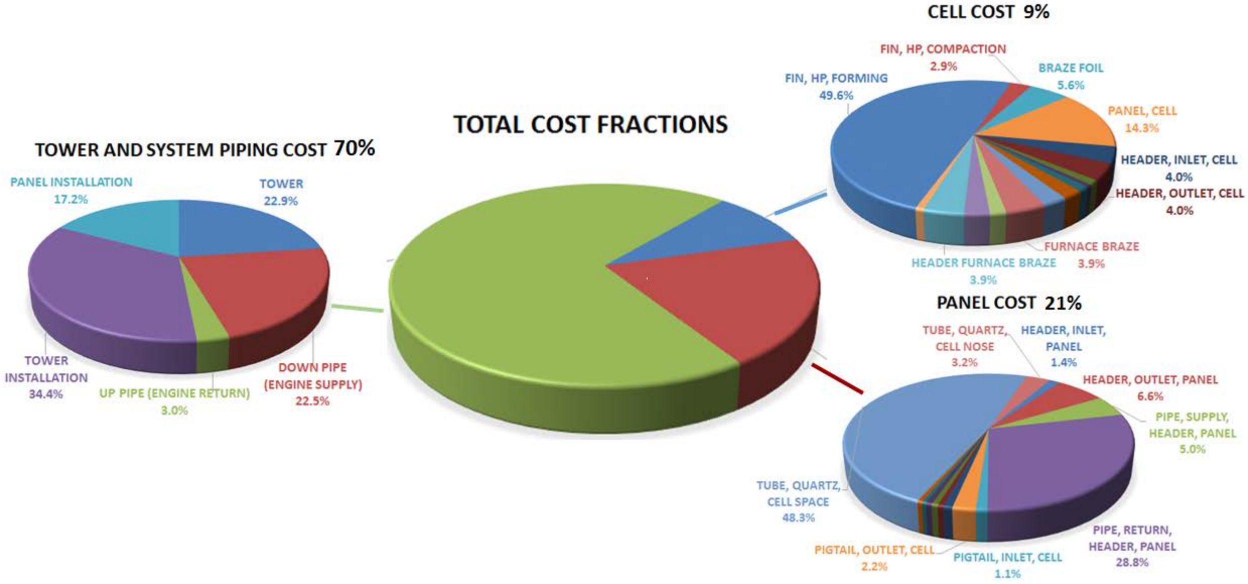

Figure 87 – Breakdown of the receiver and tower costs.

Conclusions

Brayton Energy's "High-Efficiency Low-Cost Solar Receiver for use in a Supercritical CO_2 Recompression Cycle" program resulted in the analysis and demonstration of a novel low-cost high-effectiveness heat exchanger cell architecture that is capable of operating at high temperatures with high fluid pressures. As such, it is suitable for use as a solar absorber surface and it is appropriate for use with supercritical carbon dioxide as the working fluid, thereby enabling direct heating for a high-efficiency sCO_2 engine cycle CSP system.

While that result is significant itself, the research and development performed under the purview of this program has far reaching implications for achieving the Department of Energy's 2020 6¢/kW LCOE target. The cell architecture, originally developed for the solar absorber application, is also compelling in other heat exchanger applications, including several that may directly impact the cost of CSP. The low manufacturing cost, compact size, highly effective performance, and high temperature/pressure capabilities recommend them for use as

- Brayton cycle recuperators for both high-efficiency sCO_2 cycles as well as conventional aspirated gas turbine cycles
- Heat exchangers for the transfer of energy between a thermal energy system and a working fluid such as sCO_2

An ancillary outcome of this program was the continued development of Brayton Energy's low-cost quartz tube window, which was demonstrated to have a profound performance benefit when it applied to an external receiver. Efficiency gains of more than five points were demonstrated with the addition of Brayton's window design, a result of both convection and radiation losses being significantly reduced. Note that this technology may be applied not only to the new receiver concept developed in this program, but also to conventional and state-of-the-art designs, including those already in the field, thereby significantly improving their performance and reducing the LCOE of system already operating.

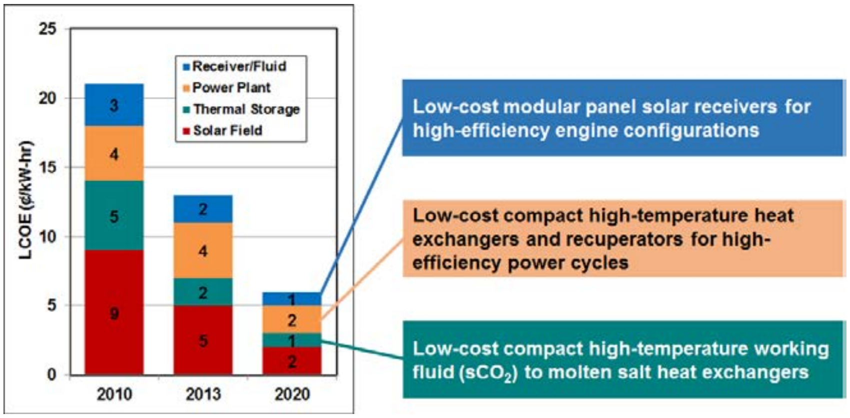

Low-cost modular panel solar receivers for high-efficiency engine configurations

Low-cost compact high-temperature heat exchangers and recuperators for high-efficiency power cycles

Low-cost compact high-temperature working fluid (sCO_2) to molten salt heat exchangers

Figure 88 – Path forward to a 6/kW LCOE, as defined in the 2012 Department of Energy Vision Study. Note that of the 4 areas identified, the success of this program may directly reduce the LCOE contribution of 3 of them by reducing capital costs, reducing space/weight requirements, and improving efficiency. The 4th area, the Solar Field, may also be indirectly improved in that increasing the overall efficiency (through the use of a quartz tube window and/or direct heating of the working fluid, thereby eliminating intermediate heat exchanger) may reduce the required heliostat field by some fraction.

Consequently this program which was originally conceived to reduce the LCOE is one area – i.e. the solar receiver – can significantly reduce costs in other areas in the DoE Vision Study. This breadth of applicability can be seen graphically in Figure 88.

Budget and Schedule

Brayton's program extended – due to increases in project scope, unforeseen challenges with some tasks, and interphase SOPO negotiations – from its initial 36-month duration (September 2012 – August 2015) to a total of 40 months. However, it should be noted that this increase in program length was still accomplished within the original $3,150,316 budget. This cost was split 50/50 between the government and Brayton.

References

[i] "SunShot Vision Study," Department of Energy, February 2012. http://www1.eere.energy.gov/solar/pdfs/47927.pdf

[ii] V. Dostal, M.J. Driscoll, and P. Hejzlar, A Supercritical Carbon Dioxide Cycle for Next Generation Nuclear Reactors," MIT-ANP-TR-100, March 10, 2004

[iii] "SolTrace Optical Modeling Software," National Renewable Energy Laboratory, August 2012. http://www.nrel.gov/csp/soltrace/

[iv] Sargent & Lundy LLC Consulting Group, "Assessment of Parabolic Trough and Power Tower Solar Technology Cost and Performance Forecasts, Chicago, IL, October 2003, NREL/SR-550-34440

[v] Manson, S.S, Mendelson, A. (1959). Optimization of parametric constants for creep-rupture data by means of least squares. *NASA Memo 3-10-59E.*

[vi] Rohsenow, W.M. and Choi, H.Y. (1961). Heat, Mass, and Momentum Transfer. Pg 211.